Buoyancy- to inertial-range transition in forced stratified turbulence

By GEORGE F. CARNEVALE[1], M. BRISCOLINI[2]
AND P. ORLANDI[3]

[1] Scripps Institution of Oceanography, University of California, San Diego, La Jolla,
CA 92093-0225, USA

[2] IBM Italia S.p.A., Via Shangai 53, 00144 Roma, Italy

[3] Dipartimento di Meccanica e Aeronautica, University of Rome, 'La Sapienza',
via Eudossiana 18, 00184 Roma, Italy

The buoyancy range, which represents a transition from large-scale wave-dominated motions to small-scale turbulence in the oceans and the atmosphere, is investigated through large-eddy simulations. The model presented here uses a continual forcing based on large-scale standing internal waves and has a spectral truncation in the isotropic inertial range. Evidence is presented for a break in the energy spectra from the anisotropic k^{-3} buoyancy range to the small-scale $k^{-5/3}$ isotropic inertial range. Density structures that form during wave breaking and periods of high strain rate are analysed. Elongated vertical structures produced during periods of strong straining motion are found to collapse in the subsequent vertically compressional phase of the strain resulting in a zone or patch of mixed fluid.

1. Introduction

Much of the large-scale variability in the atmosphere and oceans can be described as internal wave activity, while isotropic turbulence dominates at small scales. Between these extremes, the dynamics is a competition between waves and turbulence. The nature of this intermediate range, called the buoyancy or the saturation range, is highly controversial. A direct numerical simulation which could faithfully span the full range of the scales involved would be a great benefit; however, such simulations remain impractical because of the large range of scales that would need to be represented. On the other hand, as we shall argue below, techniques of large-eddy simulation (LES) should afford us the possibility of at least simulating flow in the buoyancy range and capturing the transition to the inertial range. The goal of this paper is to present some results that might confirm this hope and also give us some insight into the kinds of structures one should be able to observe in the density field of the buoyancy range.

To be concrete about spatial scales, we will concentrate on the oceanic application, although much of the basic ideas that follow should hold for the atmospheric problem as well. The spectra of density and velocity fluctuations in the ocean have several distinguishable ranges. As a guide to these ranges, we follow the description in Holloway (1981) and use a similar schematic diagram (figure 1). Here ϕ represents either the spectrum of the vertical shear or the vertical gradient of temperature as a function of the vertical wavenumber k_z. The axis of the vertical wavenumber is
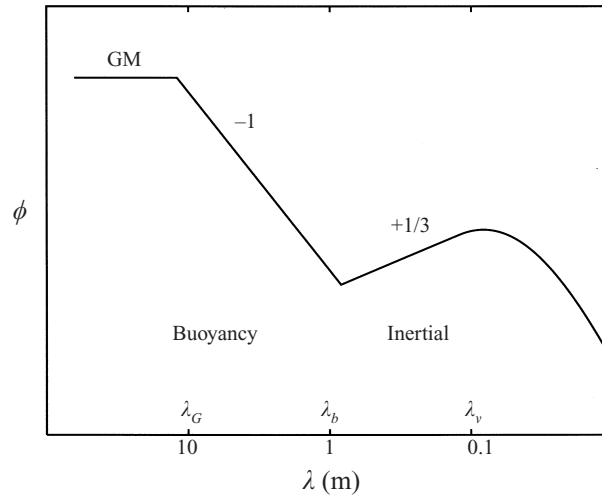
FIGURE 1. Schematic of the oceanic horizontal shear spectrum. The horizontal axis is labelled in terms of wavelength for convenience, but it is actually the k_z wavenumber axis. The slopes corresponding to the k_z^{-1} buoyancy range and the $k_z^{1/3}$ inertial range are labelled by the exponents.

labelled in terms of vertical wavelengths $\lambda = 2\pi/k_z$. Internal wave activity dominates the variability in the ocean for vertical scales from kilometres down to λ_G, which is $O(10\,\text{m})$. For this range of vertical scales, and for even much larger horizontal scales, the shear and vertical density gradient spectra seem to be well described by the Garrett & Munk (1975) (GM) spectra. This wave regime is dominated mainly by linear wave propagation for vertical scales with λ greater than about 60 m (Holloway 1980), while for scales from 60 m down to about 10 m, nonlinear wave–wave interactions are important for generating even smaller scales of motion; however, the waves of vertical scale larger than λ_G are not strong enough to overturn, that is not strong enough to transfer heavy fluid above light fluid. The waves of vertical scale less than λ_G that are produced by the nonlinear interaction of larger scale waves have amplitudes sufficiently large to cause shear instability and overturning. These waves thus create regions of instability in which there is generation of turbulence. This 'breaking' of the waves below λ_G drains energy from them and hence the fall off of the spectrum. At scales from $O(10\,\text{m})$ to $O(1\,\text{m})$, the vertical gradient spectra fall off like k_z^{-1}. This is the buoyancy range, terminating at the buoyancy or Ozmidov scale λ_b, which can be thought of as the scale of the overturning structures. The Ozmidov scale forms the boundary between the transitional buoyancy range and the turbulent inertial range. The inertial range terminates in the dissipation range for scales of a few centimetres and below.

It is difficult to model analytically the transition from the buoyancy to inertial range. In part, this is because the buoyancy range is very anisotropic, while the inertial range is isotropic, and thus a full description of the transition would really require a three-dimensional wavevector space framework. However, to make progress, theoretical arguments have tended to represent both spectra depending only on wavenumber k. The model for the kinetic energy spectrum in the buoyancy range is then

$$E(k) = \alpha N^2 k^{-3} \tag{1.1}$$

where α is an empirical constant and N is the Brunt–Väisälä frequency, which mea-

sures the strength of the stratification. The Brunt–Väisälä frequency is defined by

$$N^2 = -\frac{g}{\rho_0}\frac{\partial \bar{\rho}}{\partial z}, \tag{1.2}$$

where g is the acceleration due to gravity, $\bar{\rho}$ is the background density profile, assumed stable (i.e. $\partial \bar{\rho}/\partial z < 0$), and ρ_0 is the volume average of $\bar{\rho}$.

From the observed spectra of vertical shear, the constant α is determined to be about 0.47, but it will be more convenient for us to consider the two components of the horizontal velocity (u, v) separately, and, assuming horizontal isotropy in the observations, this would suggest $\alpha \approx 0.2$ for the spectrum of either component (cf. Gibson 1986; Gargett *et al.* 1981).

The inertial-range kinetic energy spectrum is given by

$$E(k) = C_K \epsilon^{2/3} k^{-5/3} \tag{1.3}$$

where ϵ is the turbulent dissipation rate of total kinetic energy and C_K is the empirical Kolmogorov constant. A reasonable value to assume for C_K is 1.5 (cf. Lesieur 1997). For the energy of one component of the velocity field, there would simply be a prefactor of 1/3 multiplying this isotropic spectrum. The Ozmidov (or buoyancy) wavenumber is then estimated by simply matching these two spectra at wavenumber k_b. The result is, up to an order one multiplicative constant,

$$k_b = \sqrt{N^3/\epsilon} \tag{1.4}$$

(cf. Holloway 1981; Gibson 1986).

The model for the potential energy spectrum in the buoyancy range is similar to that for the kinetic energy spectrum. The empirical constant α for the temperature spectrum is found to have value of about 0.2 (cf. Gibson 1986; Gregg 1977). The spectral model for the inertial range of density fluctuations is the Corrsin–Obukhov spectrum, which involves the decay rate of density fluctuations as well as ϵ. For our purposes, we prefer to write the spectrum directly in terms of the turbulent decay rate of potential energy, which we shall write as ϵ_{pe}. Then the Corrsin–Obukhov spectrum for the potential energy takes the following form:

$$PE(k) = C_o \epsilon_{pe} \epsilon^{-1/3} k^{-5/3}, \tag{1.5}$$

where C_o is the Corrsin constant.

Since the range of scales represented by the full spectrum covering the GM range down to and including the dissipation range is far greater than we could hope to simulate, we attempt a simulation of the buoyancy range and its transition to the inertial range by modelling the large-scale forcing and the effect of the subgrid scales. There have been a number of recent investigations involving internal-wave breaking that have used a variety of forcings and subgrid-scale models. Siegel & Domaradzki (1994) produced simulations of decaying, randomly generated stratified turbulence that captured the k_z^{-1} shear spectrum with a Smagorinsky SGS model. Kaltenbach, Gerz & Schumann (1994) provide a detailed study of shear-driven stratified turbulence using a finite difference LES model with a dynamically evolving SGS parameterization. Winters & d'Asaro (1997) performed a study using a hyperviscosity involving sixth-order spatial derivatives. They did this on an anisotropic grid that allowed them to consider energy transfers over a vast range of scales. Werne & Fritts (1999) have presented a high-resolution study of stratified shear turbulence producing inertial and dissipation ranges. Bouruet-Aubertot, Sommeria & Staquet (1996) performed decay numerical experiments in which the initial condition was a standing wave.

Closely related to that work are the analytical and experimental studies of Benielli & Sommeria (1996, 1998) on the excitation and breaking of internal waves by parametric instability. A different experimental configuration that maintains a standing wave is used by McEwan (1983*a*, *b*) and Taylor (1992), and this provides the closest laboratory example of the kind of forcing that we have used in our simulations. The numerical studies of wave breaking by Fritts, Garten & Andreassen (1996), Andreassen *et al.* (1994), Fritts, Isler & Andreassen (1994), and Isler *et al.* (1994) have done much to illuminate the nature of internal wave breaking using an SGS model in spectral space. More recent work by Andreassen *et al.* (1998) and Fritts, Arendt & Andreasson (1998) has provided details of the vortex wave dynamics involved in internal-wave breaking in shear flows. The numerical simulations most similar to what will be presented here are perhaps found in the recent work of Dornbrack (1998) and Afanasyev & Peltier (1998) on stratified flow over topography. Their work is similar to ours in that localized breaking events are produced with an LES model, although of a type rather different from ours. Dornbrack (1998) concentrates on the effects of a critical layer on the propagation of internal waves produced by flow over a sinusoidal bottom. Afanasyev & Peltier (1998) show the formation of Kelvin–Helmholtz billows in the flow over a hill. Some of the structures shown in their paper are very similar to the breaking structures that we will show, but, in addition, the kind of forcing we are using also produces some rather interesting structures not observed before. All of these papers have either simply not addressed the spectral transition from buoyancy to inertial range or have not been able to capture it because their simulations have been either too dissipative, or too turbulent.

The question of the type of forcing to adopt in our model is even more complex than suggested above. Besides the combined effect of all internal waves in the GM range there are processes other than internal waves that could also contribute to small-scale variance. As pointed out by Blix, Thrane & Andreason (1990) in the context of the atmospheric problem, in addition to propagating internal waves, there are the effects of two-dimensional turbulence, strongly layered phenomena and Kelvin–Helmholtz instabilities etc. Nevertheless, here we will use a forcing that is an oversimplification of the problem. We will limit ourselves to considering only the effect of the internal waves of the GM spectrum on the buoyancy range, and, even with that simplification, the representation of the forcing is beyond our capabilities because of the enormous spectral range spanned by those waves. The ultimate simplification that we will use here is to represent the effect of all the GM-range internal waves by internal waves only on the largest-scale of our computational domain. This has the advantage of forcing the flow with the same temporal behaviour as the waves that drive the buoyancy range in the real ocean. Also by forcing at only the largest scale of the domain, we have no sources of energy at scales in the buoyancy or inertial ranges that may cause some contamination of the results. In addition, the amplitude of the forcing wave is maintained at the same value throughout the simulation to avoid the transient effects that may be found in decay experiments. With this kind of forcing, long-term runs are possible to obtain stationary statistics. Furthermore, as will be explained in detail in §2, we have chosen to represent the forcing by a standing internal wave. In this model, the wave breaking that we are interested in occurs repeatedly, at approximately the same position, which makes defining various regions of the flow practical. It is not that we imagine the actual forcing of the buoyancy range to be a standing wave, although such a pattern could be set up temporarily by the interaction of travelling waves groups; rather this is a convenient model that we

can use to force with the internal wave temporal behaviour and at the levels of strain and shear that we may imagine forces the real buoyancy range.

There is a variety of subgrid-scale (SGS) models, that could be used for stratified turbulence. Since problems with anisotropic turbulence SGS models are still not well resolved, the most trustworthy models, from a theoretical, numerical and historical point of view, are those that have the numerical small-scale cutoff anchored in an isotropic inertial range, where the scaling on which such subgrid-scale models rely is well founded. For the oceans, this means that our best chance for faithful results in terms of correct energy transfer is to put our numerical cutoff within the range from about 1 m to about 10 cm, and to use only an isotropic grid. So our strategy will be to model a cube of the ocean in which the forcing is only internal waves in the GM spectrum with the small-scale cutoff in the inertial range.

As explained in detail in §2, the specific SGS model that we will use is the 'cusp model', and the form of simulation used is spectral. The results regarding the spectral transition from buoyancy to inertial range are discussed in §3. Interesting density and flow structures found in the simulation of the buoyancy range will be presented in §4. An investigation of the sensitivity of the results to the changes in the SGS model will be presented in §5.

2. The numerical model

For the range of parameters involved in our studies, the Boussinesq approximation is appropriate. Following the notation of Herring & Metais (1992) with regard to dissipation, the evolution equations may be written as

$$\frac{\partial \boldsymbol{u}}{\partial t} + \boldsymbol{u} \cdot \nabla \boldsymbol{u} + \frac{1}{\rho_0} \nabla p' - \frac{\rho'}{\rho_0} \boldsymbol{g} = v(\nabla^2)\nabla^2 \boldsymbol{u}, \tag{2.1}$$

$$\nabla \cdot \boldsymbol{u} = 0, \tag{2.2}$$

$$\frac{\partial \rho'}{\partial t} + \boldsymbol{u} \cdot \nabla \rho' + w\frac{\partial \bar{\rho}}{\partial z} = \kappa(\nabla^2)\nabla^2 \rho', \tag{2.3}$$

where $v(\cdot)$ and $\kappa(\cdot)$ are considered functions of the Laplacian operator and are used to represent eddy parameterizations in general, and $\boldsymbol{g} = -g$. We have neglected the effect of rotation, which should not play a significant role at the small scales with which we are concerned. The total density is given by

$$\rho = \bar{\rho}(z) + \rho'(x, y, z, t), \tag{2.4}$$

where $\bar{\rho}(z)$ is the horizontally averaged background density assumed constant in time, and $\rho'(x, y, z, t)$ is the deviation from that mean; ρ_0 is the average of $\bar{\rho}(z)$ over z. The pressure p' is the deviation from the background mean pressure; it can be determined in terms of $\boldsymbol{u}$ by taking the divergence of (2.1) under the assumption that the velocity field is divergenceless.

We simulate these dynamical equations with a spectral code with triply periodic boundary conditions. The code is based on the method of Patterson & Orszag (1971) for de-aliasing a pseudo-spectral code. The time-stepping algorithm used to advance the velocity field is a second-order leap-frog scheme. This code is conservative, that is total energy is conserved if no viscosity or diffusivity is applied and if the time step is taken sufficiently small. See Briscolini & Santangelo (1992) for further details. As a subgrid-scale parameterization, we have used the large-eddy simulation model of Lesieur & Rogallo (1989), which is based on the eddy viscosity theory
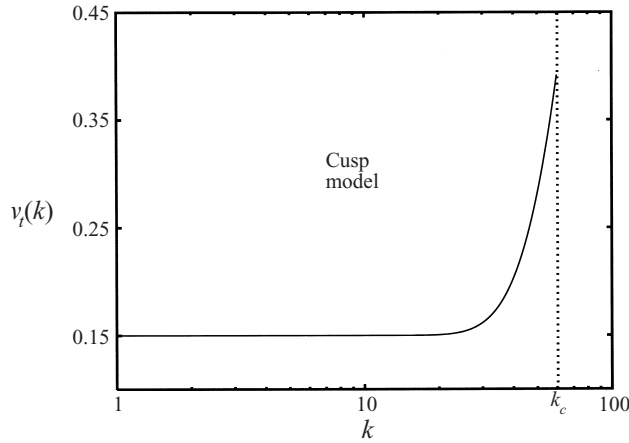
FIGURE 2. Graph of the eddy viscosity divided by $(E(k_c)/k_c)^{1/2}$, where k_c is the numerical cutoff or truncation wavenumber.

of Kraichnan (1976). This model is referred to as the cusp model since the eddy viscosity (a function of wavenumber) has a cusp-like behaviour at the highest allowed wavenumber, the spectral cutoff k_c. The eddy viscosity $v_t(k)$ can be defined by use of two-point Markovian closure theory (cf. Kraichnan 1976; Chollet 1985). The idea is to design an eddy viscosity that depends on wavenumber in such a way that it will withdraw from each wavenumber band the amount of energy that would have been passed to wavenumbers higher than k_c if there were no upper wavenumber cutoff. For unstratified turbulence, there is an approximation based on assuming k_c is in the inertial energy range that has proven satisfactory. This approximation is

$$v_t(k) = (a_1 + a_2 \exp(-a_3 k_c/k)) \sqrt{E(k_c)/k_c}, \qquad (2.5)$$

where the a_i are constants and $E(k)$ is the isotropic energy spectrum. This model results from assuming that the correct energy spectrum in the inertial range will take a $k^{-5/3}$ form. Hence, if the energy in the flow is sufficiently high that eddy viscosity dominates over molecular viscosity, then the eddy damping will be such as to favour the formation of a $k^{-5/3}$ range. The study of Lesieur & Rogallo (1989) suggests the optimal choices for the coefficients a_i for the problem of truncating an infinitely long inertial range. In general, the best choice of the coefficients will depend on the extent of the inertial-range spectrum being modelled (Chollet 1985). In our work, however, we have simplified things by just fixing the choice for these parameters for all simulations. We have used the values Lesieur & Rogallo (1989) found appropriate for a 64^3 simulation of infinite Reynolds number turbulence. Specifically, we take $a_1 = 0.15$, $a_2 = 5$ and $a_3 = 3.03$. In figure 2, we show a graph of v_t normalized by $\sqrt{E(k_c)/k_c}$. Note that there is a long plateau for large scales with the value $v_{t0} = a_1 \sqrt{E(k_c)/k_c}$. This is the eddy viscosity that acts on large scales due to subgrid-scale eddies. It seems reasonable in modelling the buoyancy range to use such a model since it does not completely neglect the effects of unresolved eddies on the buoyancy range, but, at the same time, it puts the strongest eddy viscosity in the inertial range near the cutoff. Note that the spectral cutoff that we use is isotropic, that is all wavevectors in any direction of wavenumber greater than k_c are eliminated, thus avoiding any anisotropic artifacts due to the truncation.

We should emphasize the point that the size of the eddy viscosity depends on the
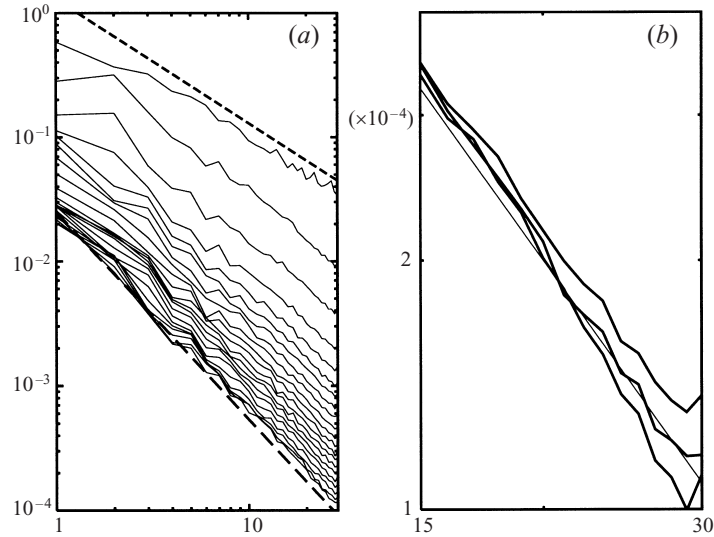
FIGURE 3. (*a*) Graphs of the potential energy spectra during a decay experiment (64^3). The thick dashed straight lines indicate $k^{-5/3}$ and k^{-1} spectra. (*b*) The potential energy spectrum for three decay experiments differing only in the turbulent Prandtl number. The lower/middle/upper spectrum corresponds to the choice $Pr_t = 0.50, 0.55, 0.60$. The thin straight line indicates a $k^{-5/3}$ spectrum. The *x*-range is $k = 15$ to $k = 30$.

amount of energy at the cutoff scale. If the resolution of the simulation of a given physical flow is increased, that is if k_c is increased, then the eddy viscosity will be correspondingly smaller. The total viscosity used in the simulations is the sum of the eddy viscosity (2.5) and the constant molecular viscosity v_{mol}. Thus the $v(\nabla^2)$ in equation (2.1) in the spectral simulation is taken as the total viscosity:

$$v(k) = v_{mol} + v_t(k). \tag{2.6}$$

Therefore, if we imagine a sequence of simulations of increasing resolution for a flow with the same large-scale forcing, the eddy viscosity will become smaller and smaller compared to the molecular viscosity. For $k_c > k_\eta$, the eddy viscosity will be insignificant, and the simulation will be equivalent to a fully resolved DNS (direct numerical simulation) with molecular viscosity alone.

The choice of turbulent diffusion depends on the choice of values for various parameters that enter into the turbulence closure model for stratified turbulence. Chollet (1985) (see also Lesieur & Rogallo 1989) found that $\kappa_t(k)$ is similar to $v_t(k)$ to the extent that it also has a plateau at small k and a cusp at the spectral cutoff. The value of the turbulent Prandtl number $Pr_t \equiv v_t/\kappa_t$ as a function of k for one set of closure model parameters was found to vary from about 0.5 to 0.6. For simplicity, we have just taken $Pr_t(k)$ to be a fixed constant independent of k in our simulations. We determined this constant by examining the evolution of the potential energy spectrum for decaying stratified turbulence that is initially highly excited at all scales. More specifically, we started with an initial spectrum in which the GM spectrum was continued to scales below 10 m as in the decay simulations of Siegel & Domaradzki (1994). With $Pr_t = 0.55$ our simulations of decaying turbulence produced spectra with the high wavenumbers obeying the $k^{-5/3}$ law for both velocity and density fluctuations. In figure 3(*a*), we show the resulting evolution of the potential energy spectrum for one such run with resolution 64^3. The initial, randomly generated spectrum, has a

spectral form close to k^{-1} for large k. This quickly decays, and eventually the spectrum is nearly $k^{-5/3}$ from about $k = 5$ to $k = k_{max} = 30$. The evolution represented spans a time of $\Delta t = 10/N$, or in terms of the time-averaged enstrophy during the evolution, this represents 100 eddy turnover times with the turnover time defined as the inverse square root of the average enstrophy. The details of the high-wavenumber potential energy spectra for the three test cases $Pr_t = 0.5$, 0.55, and 0.6 are shown in 3(b). The jump in energy in the last wavenumber band is typical for the cusp model, and indicates failure to sufficiently dissipate energy at the very end of the spectrum. Based on these tests, we adopted $Pr_t = 0.55$ for all of the simulations reported here.

Of course, there are many criticisms one could make about the use of LES, particularly for evolving flows. In a recent paper, Woodruff, Shebalin & Hussaini (1999) attempt to provide a criterion for the closeness of fit between some DNS and LES statistics in evolving flows based on several LES models. They found that when a Reynolds number defined by $Re_\epsilon \equiv \Delta^2 S_0/v_{mol}$, where Δ is the grid spacing and S_0 is the large-scale strain rate, is $O(1)$ then the LES will be a good approximation to DNS results. In the simulations to be presented below, we use a fixed value of S_0 based on some oceanographic parameters, and choose either $v = 0$ or $v = 0.01\,\mathrm{cm^2\,s^{-1}}$, which choices lead to $Re_\epsilon = \infty$ and $Re_\epsilon \approx 7$, respectively. Thus the former case fails and the latter case reasonably well satisfies this criterion. On the other hand, Chollet (1985) observes that universal SGS models rely on the existence of a long inertial range which suggests that the higher the Reynolds number, the better the LES model could be expected to perform. At the same time it also means that any finite Reynolds number flow would theoretically require an ad hoc parameterization that takes into account the actual length of the inertial range beyond the truncation wavenumber. These issues are yet unsettled, and the case of stratified flow has been far less the object of study than unstratified flow. So, it should be born in mind when applying LES to any stratified flow that there are many questions concerning the validity of the approach that are still unresolved.

Next we turn to the question of the forcing. The large-scale flows that actually drive the buoyancy range are predominantly the waves of the GM range. The full range where internal wave dynamics dominates includes scales of kilometres in the horizontal and hundreds of metres in the vertical. Because of lack of resolution, we cannot provide a full representation of the effects of all large-scale internal wave forcing on the buoyancy range. In our model, of necessity, we perform a drastic reduction in modelling the forcing; we replace the driving of all of the GM waves by a linear standing wave at one wavelength. As mentioned in the introduction, Bouruet-Aubertot, Sommeria & Staquet (1995, 1996) in two-dimensional simulations of a stratified turbulence excited a standing wave of the type we use, but they allowed this wave to decay, while we maintain its amplitude.

To give the form of the forcing used, let us first introduce non-dimensional units. We will take all lengths to be scaled by $2\pi/L$, where L is the length of one side of our computational domain. Time will be scaled by $1/N$. Then the frequency of linear internal waves is given by

$$\sigma = \pm \frac{k_h}{k}, \tag{2.7}$$

where $k_h = \sqrt{k_x^2 + k_y^2}$ is the horizontal wavenumber. One particular linear standing wave is

$$\boldsymbol{u} = (u, v, w) = A \frac{g^*}{\sqrt{2}}(0, \sin y \sin z, \cos y \cos z) \sin \frac{t}{\sqrt{2}}, \tag{2.8}$$
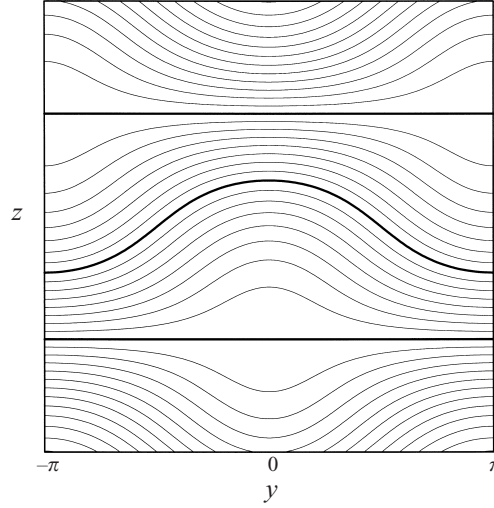
FIGURE 4. Contour plot of the density field in a vertical y, z cross-section through the centre of the domain. The width and height of the cross-section are each 20 m. The instant shown corresponds to maximum displacement of the isopycnals for the forcing of strength $S_{GM}(20\,\text{m})$ as discussed in §3. The upper and lower flat thick contour lines are the isopycnals corresponding to the two nodal planes of the forcing. The curved thick line is the isopycnal that is most strongly disturbed by the forcing and corresponds to $\rho = \rho_0$. The contour interval is $\pi N^2/16g$.

$$\frac{\rho'}{\rho_0} = A \cos y \cos z \cos \frac{t}{\sqrt{2}}, \tag{2.9}$$

where A is an arbitrary amplitude and g^* is the non-dimensional gravity. Note that the dimensional period of this wave, which is the forcing period, is given by

$$T_F = \sqrt{2}\frac{2\pi}{N}. \tag{2.10}$$

To give some idea of the structure of this standing wave, we show in figure 4 a contour plot of the density field in a vertical y, z cross-section. Note that the density field in this standing wave has no variation along the x-direction. In this figure, we see an instantaneous representation of the iso-density surfaces. When $t/\sqrt{2}$ is an odd multiple of $\pi/2$, these isopycnals will all be flat. The degree to which they deviate from that at other times depends on the value of A as well as t. The instant of time represented here is such that $t/\sqrt{2}$ is an integer multiple of π and, hence, one of maximum distortion of the density contours. Note however that the density field in (2.9) has two nodal planes, represented by two thick contour lines in the figure, at $z = \pm\pi/2$ (non-dimensional). During the forcing cycle, these planes remain flat and fixed in position. The fluid above and below these planes vertically approaches and retreats from them depending on the phase in time and the y-position considered. Thus the points on the nodal planes at $y = 0$ and $y = \pm\pi$ are the centres of regions of oscillating high strain. For example, at the instant represented, consider the point $y = 0$ on the upper nodal plane. The currents in the vicinity of this point have advected fluid vertically toward the nodal plane from both above and below, while in the horizontal y-direction fluid has been advected to the left and right away from $y = 0$. Thus, at this point on the nodal plane, at this time, the sense of the strain is compressional in the z-direction and dilational in y. The point on the upper nodal plane at the edge of the domain ($y = \pm\pi$, recall the field is periodic) is in a region of high strain of the

opposite sign, with the vertical direction being dilational and the horizontal direction being compressional. On the lower nodal plane, we see that it is the $y = 0$ point that is in a region of vertical 'dilation' and the edge in a region of vertical 'compression'. In terms of the density field, these points are centres of regions of high/low vertical density gradients relative to the mean gradient. Also we should note that the instant represented is one of maximal magnitude of strain at these points, but that the vertical strain rate $\partial w / \partial z$ is zero everywhere because the motion of the density contours off the nodal lines has just come to a halt and is about to change direction. The thick contour line lying between the two nodal planes represents the most perturbed isopycnal at the time of its greatest deviation from a flat surface. How the amplitude of the standing wave is chosen for our simulations is discussed in the next section.

In two-dimensional numerical studies of Bouruet-Aubertot *et al.* (1996), the standing wave becomes unstable and generates turbulence. This would also happen in our three-dimensional simulation, but the turbulence would be highly constrained since there is as yet no source of x-variation in our flow. To break the two-dimensional symmetry of the flow, while maintaining the basic structure of the large scale, we add a weak component of forcing with x-variation. We have tried this in various ways: adding a random initial perturbation at all scales, randomly forcing the modes with $k = 1$ at each time step, adding another large-scale standing wave, adding a propagating wave, and so on. The results are similar to each other if the perturbations are sufficiently weak. For the simulations discussed below, we have added to the primary forcing wave only a small-amplitude standing wave of the same scale. Specifically, we added the following perturbation:

$$\boldsymbol{u} = A' \frac{g^*}{\sqrt{2}} (\cos(x + z), 0, -\cos(x + z)) \sin \frac{t}{\sqrt{2}}, \qquad (2.11)$$

$$\frac{\rho'}{\rho_0} = A' \cos(x + z) \cos \frac{t}{\sqrt{2}}. \qquad (2.12)$$

Thus in the simulations discussed below the forcing occurs only at $k = \sqrt{2}$. The coefficient A' was taken to be $A/20$, and, hence, the energy in the perturbation is only $1/400$ that of the primary forcing wave.

3. Numerical experiments

With the numerical model presented above, we performed a series of experiments in which the size of the computational domain and the amplitude of the forcing were varied. The initial studies were at resolution 64^3 and showed that for sufficiently large amplitudes A for which the forcing wave itself was overturning, a $k^{-5/3}$ spectrum extending over most of the spectral range could be established. For weaker forcing, a steeper spectrum approximating k^{-3} was found (Carnevale & Briscolini 1999). For intermediate-amplitude forcings, we were able to observe, at least intermittently, cases which do appear to exhibit the transition from the buoyancy range to the smaller-scale inertial range. Weak and strong forcings are measured relative to shear amplitudes typical in the thermocline. The best results were obtained with a forcing amplitude that could actually be considered representative of wave amplitudes in the thermocline. Specifically, the forcing amplitude that we refer to as intermediate, is for a value of A in equations (2.8) and (2.9) such that the maximum shear during a cycle of the forcing is equivalent to the r.m.s. shear of the GM spectrum at the scale of our computational domain. The r.m.s. shear is calculated by integrating the shear of

the GM spectrum from the kilometre scale down to the scale of interest (cf. Gregg 1989). Our best results tended to be for cases in which the vertical wavelength of the forcing was 20 m. For $N = 3$ c.p.h., the net r.m.s. shear from the GM spectrum for this scale is $S_{GM}(20\,\text{m}) \approx 3 \times 10^{-3}\,\text{s}^{-1}$ (cf. Gregg 1989). Taking this value to determine the amplitude of our forcing, we obtain a standing wave in which the largest deviation of the density isosurfaces is as illustrated in figure 4. Thus we have a standing wave that does not itself overturn during the forcing cycle, and, in addition, the Richardson number of the forcing wave, defined by

$$Ri \equiv -\frac{\dfrac{g}{\rho_0}\dfrac{\partial \rho}{\partial z}}{\dfrac{\partial u}{\partial z}^2 + \dfrac{\partial v}{\partial z}^2} \qquad (3.1)$$

does not drop below 3.125. Therefore, the forcing wave itself is convectively stable and not subject to shear instability. This kind of forcing is consistent with the picture that the GM waves themselves are not convectively or shear unstable, but through wave–wave interactions will produce smaller scale waves that are unstable by these criteria. Choosing a stronger forcing wave that is itself convectively or shear unstable would miss the important cascade process that produces the unstable waves of the buoyancy range, but would rather produce turbulence directly resulting in an inertial range (cf. Carnevale & Briscolini 1999).

For all of the simulations discussed below, we used a resolution 128^3 and a computational cube of 20 m on a side, with the forcing amplitude fixed so that the max shear in the forced wave is $S_{GM}(20\,\text{m})$. Thus our isotropic spectral cutoff is at wavenumber 60, and the smallest resolved wavelength is about 33 cm (with grid spacing $20\,\text{m}/128 \approx 16\,\text{cm}$). In each case, the Väisälä frequency is taken to be 3 cycles per hour, which is a typical oceanic value.

A long simulation was performed with realistic values for the molecular viscosity and diffusivity. The kinematic viscosity was set to $v_{mol} = 0.01\,\text{cm}^2\,\text{s}^{-1}$ and the molecular Prandtl number at $Pr_{mol} = 7$ (cf. Gargett 1985). We can calculate a Reynolds number for the oceanic flow for vertical motions on the 20 m scale by using the r.m.s. shear. Thus we can write

$$Re = S_{GM}(L)L^2/v_{mol}. \qquad (3.2)$$

For $L = 20$ m, this Reynolds number would be approximately 10^5. By including the molecular viscosity, the simulation is an attempt to represent flow with this Reynolds number. We will see that there is not much difference with results obtained by neglecting the molecular components of viscosity (i.e. $Re = \infty$) and diffusivity. With slightly less resolution than used here, Dornbrack (1998) also found little Reynolds number dependence for a similar problem when Re is above 5×10^4. That is to say that over the range of scales simulated (20 m to 16 cm) the difference between infinite Reynolds number flow and that for $Re = 10^5$ is small. At scales smaller than those simulated here, there would, of course, be a large difference, with the infinite Reynolds number case having an inertial range extending to $k = \infty$, while the finite Reynolds number case should have a dissipation range starting presumably at a wavelength of about a few cm. We could also discuss this in terms of the Taylor-scale Reynolds number. There are several ways to calculate this number for isotropic turbulence; for example, following Frisch (1995), it is given by

$$Re_\lambda = (10/3)^{1/2}\frac{E}{\Omega^{1/2}v_{mol}}, \qquad (3.3)$$
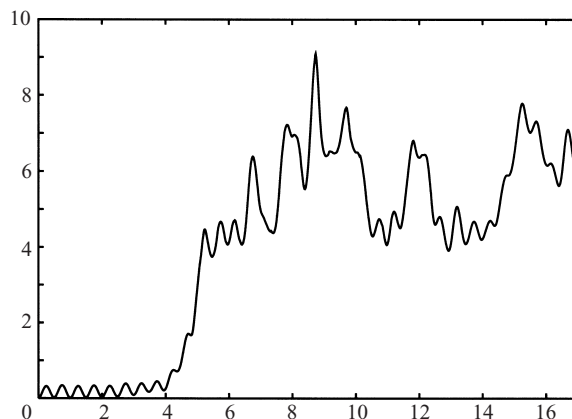
FIGURE 5. Graph of the evolution of the total enstrophy in units of N^2. The unit for the horizontal time axis is the period of the cyclic forcing, that is $\sqrt{2}\,(2\pi/N)$.

where E and Ω are the total energy and enstrophy of the flow. The Reynolds number based on the forcing scale and flow strength at the large scale is related to the Taylor-scale Reynolds number by the approximate relation $Re_\lambda \sim Re^{1/2}$ for large Re (Frisch 1995). For example, a physical flow with $Re \sim 10^5$ will have $Re_\lambda \sim 300$. Note that unlike Re, the definition of Re_λ depends on the small scale structure of the flow. Thus, although we can directly determine, Re from the resolved scales in an LES, this is not so for Re_λ which can only be inferred indirectly. For example, in the formula (3.3), Ω is the total enstrophy of the physical flow, so if we replace this with the resolved enstrophy, we will underestimate it, and thus overestimate Re_λ. Thus it is more practical from the viewpoint of these simulations to discuss Re for the flow since this can be directly determined from the resolved scales and v_{mol}, leaving Re_λ to be inferred from the asymptotic formula for high Reynolds number turbulence.

In order to understand the evolution of our forced flow, we made an animation of the evolution of the isosurface that is most distorted by the forcing ($\rho = \rho_0$) and of one of the isosurfaces corresponding initially to a nodal plane. During the early evolution, for approximately four periods of the forcing, the motion is essentially just that of the nearly two-dimensional standing wave. During this time there are only sinusoidal waves on the most disturbed isosurface, but these waves then fold over forming elongated overturns. These regions are convectively unstable and break. At this point the three-dimensionality of the flow becomes evident. The evolution of the enstrophy is a good indicator of this first breaking event. In figure 5, we see that for the first three periods of the forcing, the enstrophy is only that contained in the forcing wave itself. Then, as folds in the density surface begin to form, the mean enstrophy begins to rise, and for $t \approx 5$, the wave breaks with the production of a large amount of enstrophy. After this, the flow appears to become substantially three-dimensional on the small scale, and this is verified by the component energy spectra. The subsequent evolution of the enstrophy shows large fluctuations on which there is a smaller cyclical component with frequency comparable to that of the forcing. Although we have no runs at this resolution longer than 17 forcing periods, similar experiments at resolution 64^3 show that such fluctuations persist even after 200 forcing periods (Carnevale & Briscolini 1999).

Although it proves difficult to precisely match the enstrophy fluctuations with particular structures in the density isosurfaces, we can give some idea of the acyclic
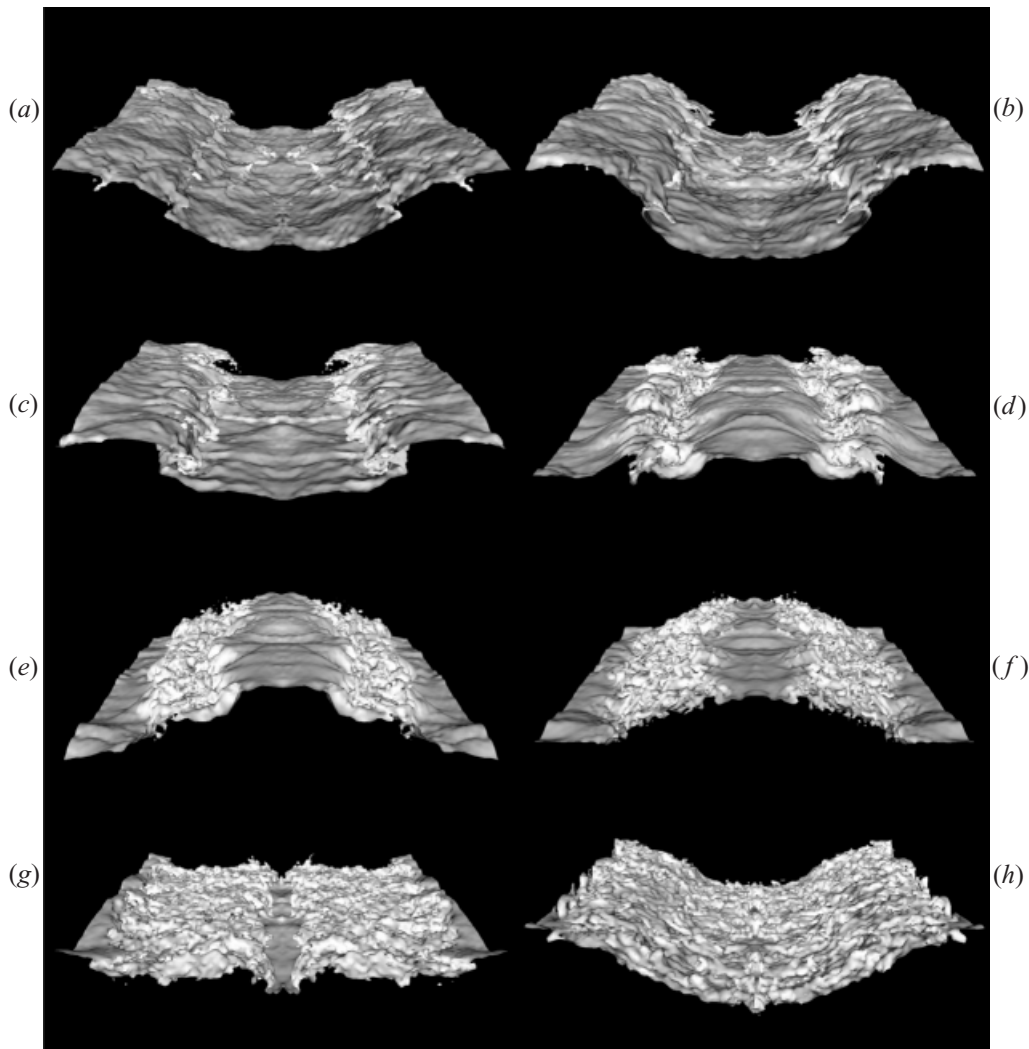
FIGURE 6. The evolution of the $\rho = \rho_0$ isopycnal during one cycle of the forcing. The frames are ordered by time from (a) to (h). The first corresponds to $t = 11.39 T_F$, the interval between frames is $\Delta t = T_F/7$.

behaviour by displaying the evolution of the $\rho = \rho_0$ surface for one cycle of the forcing. The breaks occur nearly symmetrically with large-scale overturning occurring nearly at the same values of y and z each time and along lines of constant x, respecting in the large scales the symmetry of the main part of the forcing. However, no two of the breaking events with the subsequent evolution during the forcing cycle are the same. In figure 6, for one such cycle, we show eight instantaneous images of this isosurface using a perspective three-dimensional plot. The frames are ordered temporally from (a) to (h): (a) corresponds to $t = 11.39 T_F$, and the interval between frames is $\Delta t = T_F/7$. Thus (a) and (h) correspond to the same phase of the forcing. Frame (a) captures the moment when breaking is just beginning. Let us say that (a–d) represent the breaking event, and (e–h) the aftermath. We see that during the breaking event, heavy fluid spills over lighter fluid, crashing down with the creation
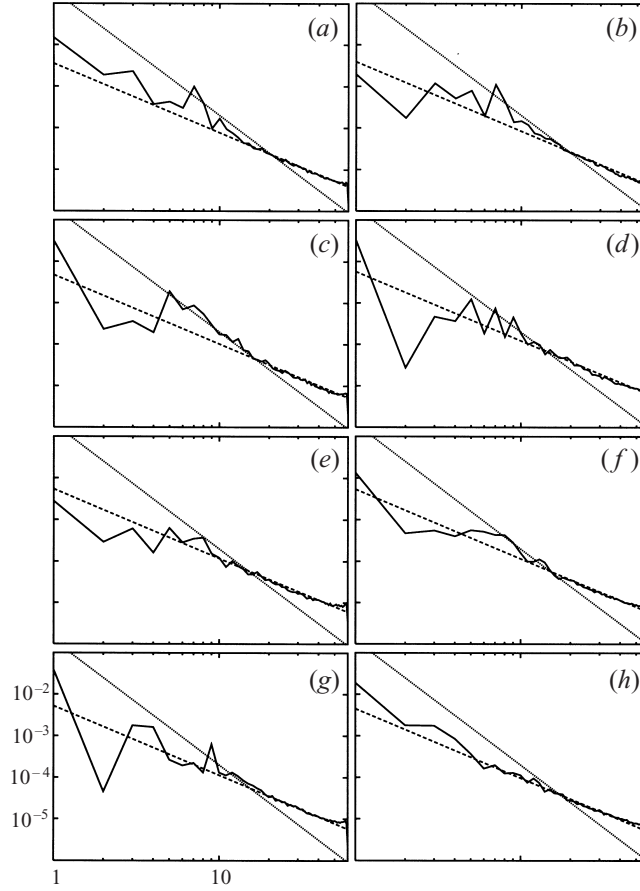
FIGURE 7. Kinetic energy spectra for the v-component of the velocity during one cycle of the forcing. In each panel the dashed line is the Kolmogorov spectrum $(1/3)C_K\epsilon^{2/3}k^{-5/3}$ with $C_K = 1.5$, and the dotted line is the saturation spectrum $0.2N^2k^{-3}$. The time interval between frames is $\Delta T_F/7$ and (*a*) corresponds to time $t = 11.39T_F$. These are log-log plots of $E(k)$ in units of $N^2(L/2\pi)^3$ vs. k in units of $2\pi/L$. All plots have the scales as indicated in panel (*g*).

of small-scale structures all along the lines of the two breaking regions. This kind of breaking appears to be very similar to that found in the laboratory experiments with standing-wave forcing (Taylor 1992; McEwan 1983*a*). Afterwards, the region of the small-scale turbulent structures spreads, eventually 'contaminating' the entire isosurface. If we compare frame (*h*) with frame (*a*), we see that the final surface is much rougher, filled with small-scale structures everywhere, and that there is no larger scale folding over of the surface as there was in the first frame. In the later evolution, the wave will break again, but only after a refractory period, in this case of about two forcing cycles. In terms of the enstrophy evolution during the breaking event and its aftermath, we see from figure 5 that figure 6(*a*) represents a relative minimum in enstrophy but then the enstrophy climbs rapidly during the breaking event, with maximum values attained around the times of figures 6(*c*) and 6(*d*). During the aftermath, the enstrophy declines rapidly, again reaching a value comparable to that at the time of figure 6(*a*), even though this density isosurface is clearly more perturbed. The nature of the later breaking events appears to depend on how much small-scale structure is present, but in none of the subsequent events was there a
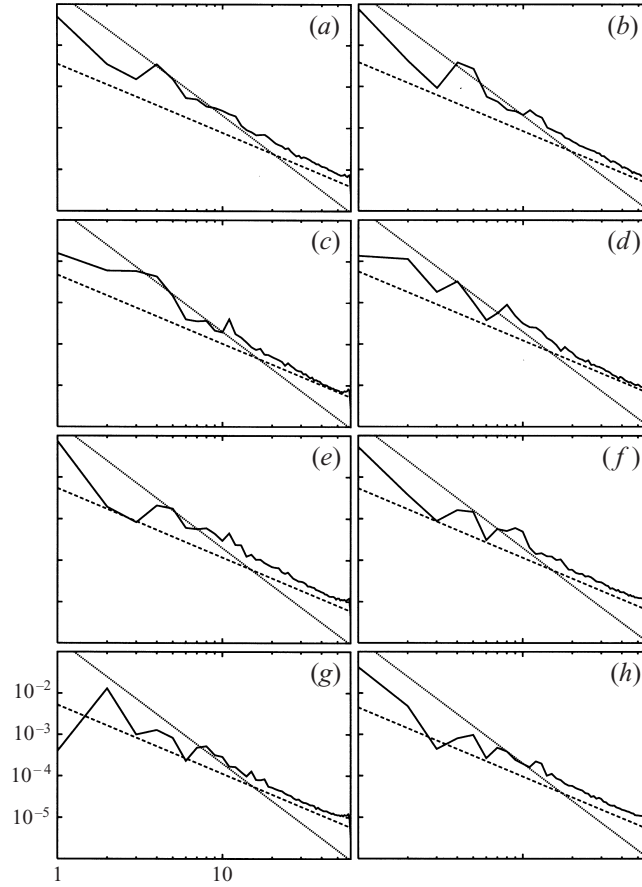
FIGURE 8. Potential energy spectra one cycle of the forcing. In each panel, the dashed line is the Corrsin–Obukhov spectrum $C_o \epsilon_{pe} \epsilon^{-1/3} k^{-5/3}$ with $C_o = 0.67$ and the dotted line is the saturation spectrum $0.2N^2 k^{-3}$. The time interval between frames is $\Delta T_F/7$ and (a) corresponds to time $t = 11.39 T_F$. These are log-log plots of $PE(k)$ in units of $N^2(L/2\pi)^3$ vs. k in units of $2\pi/L$. All plots have the scales as indicated in panel (g).

repetition of the nearly two-dimensional breaking that occurs for the first breaking event (at $t \approx 5T_F$).

Next we will consider the energy spectra for the flow at the same times as those illustrated in figure 6. Since the energy is highly anisotropic at scales larger than those in the inertial range, plotting the total energy as a function of the isotropic wavenumber tends to obscure the transition between small and large scales. To most clearly display the transition, we have found it useful to consider the spectrum of v, the y-component of velocity, which is the horizontal component that is directly affected by the forcing. The spectra, $E_v(k)$ are computed for integer wavenumbers by summing all of the modal energies $\frac{1}{2}|v_k|^2$, with k between k (inclusive) and $k + 1$ (exclusive). Thus $E_v(k = 1)$ contains the energy in the forced mode ($k = \sqrt{2}$) as well as any energy in other modes $k < 2$ achieved by mode–mode interaction. Along with the spectra, we have also drawn lines corresponding to the inertial-range spectrum $(1/3)C_K \epsilon^{2/3} k^{-5/3}$ and buoyancy-range spectrum $0.2N^2 k^{-3}$. For each frame, ϵ is taken as the total kinetic energy dissipation rate at that time. We have included a factor of $(1/3)$ which is appropriate for a single component in the isotropic inertial range. For

the Kolmogorov constant, a value of 1.5 was used in each case. We should emphasize that no attempt is made here to fit the data, but the coefficient is just taken as this standard value *a priori*. For the buoyancy-range spectrum, we have used the coefficient $\alpha = 0.2$ in all cases. In each frame shown in figure 7, we see a fairly good match at wavenumbers greater than about 20 (that is for scales below about 1 m) to the Kolmogorov inertial-range spectrum. The main deviation is at wavenumbers near $k = 60$, the cutoff wavenumber, and this is to be expected from previous experience with the cusp model (cf. Lesieur & Rogallo 1989). The spectrum below wavenumber 20 is naturally far more irregular than that above due to the much smaller number of modes in the lower spectral bands. If we neglect the first few wavenumbers, then there is some evidence here for a steeper spectral range for wavenumbers below about $k = 20$, that is for scales larger than about 1 m, at least in the frames that correspond to times during the breaking of the wave (*a–d*). In the aftermath of breaking, the spectra tend to be somewhat flatter (*e–h*). The best representative of the transition between buoyancy and inertial range is found in panel (*c*), which corresponds to a time when the enstrophy is near a local maximum. Here the buoyancy-range spectrum makes a reasonably good fit in the range of scales from about 4 m down to about 1 m. From the forcing scale (20 m vertical) to about the 5 m scale, there is a dip in the energy that has also been seen in the spectra from similar two-dimensional simulations of the decay of a standing wave (Bouruet-Aubertot *et al.* 1996). These kinetic energy spectra should be compared with the potential energy spectra in figure 8. Here the high-wavenumber parts of the spectra are to be compared with the Corrsin–Obukhov spectrum (1.5). Recalling that the potential energy in the Boussinesq approximation is given by

$$PE = \frac{1}{2}\frac{g^2}{N^2}\int \frac{\rho'^2}{\rho_0^2}\mathrm{d}^3\boldsymbol{r}, \qquad (3.4)$$

we form the non-dimensional $PE(k)$ by summing the modal values of $0.5g^{*2}|\rho'_k/\rho_0|^2$ in each k interval. An accepted value for the Corrsin constant is $C_o = 0.67$ (cf. Lesieur 1997) and this has been used in each case. The potential energy dissipation rate ϵ_{pe} is calculated separately for each time shown. Again no attempt has been made to fit the data to this spectrum. We see that the match is less good than in the kinetic energy case. It appears that the Corrsin constant is too small to match our results. Also the slope of the spectra is somewhat less well matched to a pure $k^{-5/3}$ spectrum than for the E_v spectra. Nevertheless, the $k^{-5/3}$ spectrum is still a reasonable match to the PE spectra for scales smaller than about 1 m. Again, as for the kinetic energy spectra, the buoyancy-range spectrum with the coefficient 0.2 (that is the spectrum $PE(k) = 0.2N^2k^{-3}$) is a reasonable match to the spectra for scales from about 5 m down to about 1 m. Of course there is a lot of variability in the large-scale part of the spectra; however, it seems there is evidence here for a transition from a steep buoyancy range to a shallower inertial range.

In this experiment it appears that the expected spectral signature of a transition between a buoyancy range at large scale and the inertial range at small scale occurs only for periods during which there is active breaking. Let us focus on the breaking event. Figure 6(*c, d*) are images of the $\rho = \rho_0$ isosurface at the two times identified as the best for illustrating the spectral break we are looking for. The first shows the curling over and spilling down or plunging of the heavier fluid over lighter, and the later image suggests mixing by the appearance of many small-scale structures along the two parallel lines of the breaking wave. The corresponding spectra for all three components of kinetic and for the potential energy are shown in figure 9.
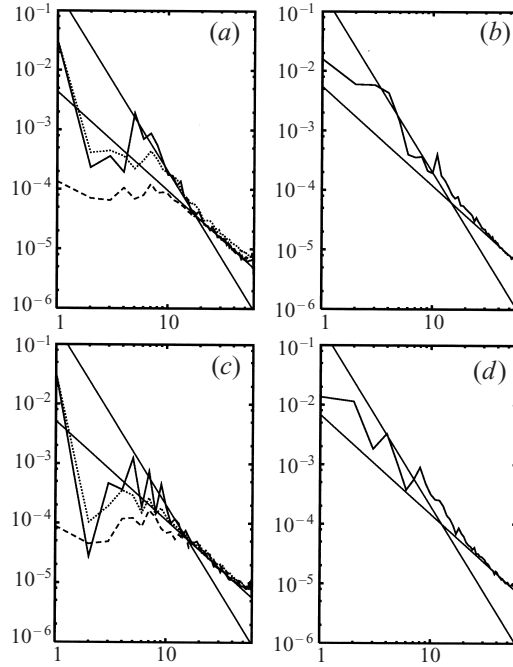
FIGURE 9. (*a*) Kinetic energy spectra for all three components of the velocity at time $t = 11.68T_F$. The thick dashed, solid and dotted lines correspond to the energy spectra for the u, v, and w components respectively. The thin solid lines correspond to the Kolmogorov spectrum $(1/3)C_K\epsilon^{2/3}k^{-5/3}$ with $C_K = 1.4$ and the saturation spectrum $0.2N^2k^{-3}$. (*b*) Potential energy spectrum at time $t = 11.68T_F$. The thick solid line corresponds to the potential energy spectrum. The thin solid lines correspond to the Corrsin–Obukhov spectrum $C_o\epsilon_{pe}\epsilon^{-1/3}k^{-5/3}$ with $C_o = 0.83$ and the saturation spectrum $0.2N^2k^{-3}$. (*c*) As in (*a*) but for $t = 11.82T_F$ and $C_K = 1.4$. (*d*) As in (*b*) but for $t = 11.82T_F$ and $C_o = 0.80$.

First we notice that although the spectra are highly anisotropic from the forcing scale (20 m) down to about the 1 m scale, there is an approximate 'return' to isotropy for the smaller scales. This is particularly evident in the kinetic energy spectra for $t = 11.82T_F$ (panel *c*). In panels (*a*) and (*c*), we have made an attempt to draw the best fit inertial-range spectra to determine the appropriate Kolmogorov constants (C_K) that fit these data. We did this for the $E_v(k)$ spectra, obtaining the best fit 'by eye' from enlarged portions of the small-scale spectra. The result that was used to draw the inertial-range model spectra in panels (*a*) and (*c*) is (C_K) = 1.4. In panels (*b*) and (*d*), the potential energy spectra are drawn. The small scales were fit to the Corrsin–Obukhov spectrum to determine the appropriate Corrsin constant. The Corrsin constants used to draw the model Corrsin–Obukhov spectrum were $C_o = 0.83$ and 0.8 respectively. In all panels the model buoyancy-range spectrum drawn is $0.2N^2k^{-3}$. Thus the Kolmogorov constant found here is somewhat smaller than the empirical values of 1.5 and the Corrsin constant is somewhat larger than the empirical value of 0.67. Nevertheless, the values are remarkably close to the empirical values, given that the spectral width of the inertial range here only covers wavelengths from about 1 m to about 33 cm. Also the near collapse of the three kinetic energy spectra for small scales at the time corresponding to the image shown in figure 6(*d*) is encouraging, and this isotropization is even better for later breaking events as we will see below. Thus it seems that the subgrid-scale model is working well at small scales
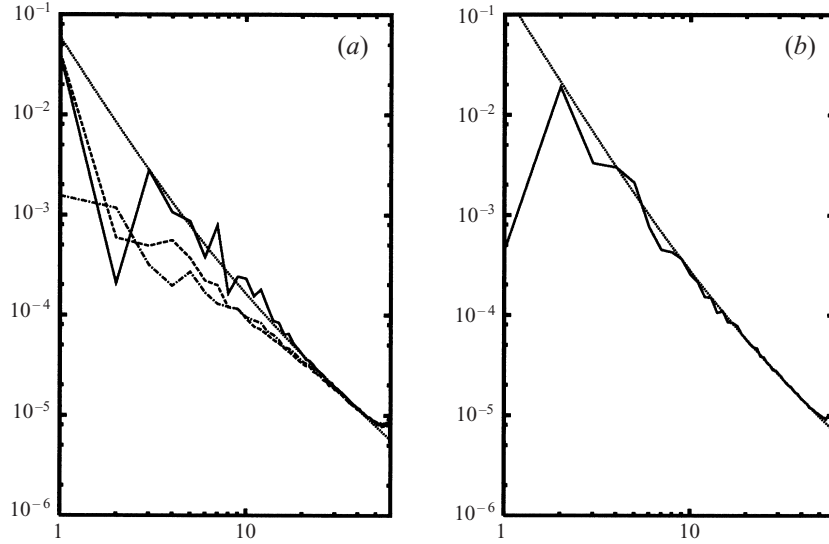
FIGURE 10. (a) Kinetic energy spectra for all three components of the velocity at time $16.8T_F$ just after a wave breaking event. The dot-dashed, solid and dashed lines correspond to the energy spectra for the u, v, and w components respectively. The dotted straight line corresponds to 1/3 of the theoretical spectrum in (3.5) with $C_K = 1.44$ and $C_u = 0.16$. (b) Potential energy spectrum at time $16.8T_F$. The solid line corresponds to the potential energy spectrum. The dotted straight line corresponds to the theoretical spectrum in (3.6) with $C_o = 0.73$ and $C_\theta = 0.16$.

and that the dynamics of the transition from anisotropic buoyancy to the isotropic inertial range is acting as imagined in theoretical models.

From this run, perhaps the best example that we have of the transition from buoyancy to isotropic inertial range occurs somewhat later, at about time $16.75T_F$. The flow at that time is approximately at the same phase of the forcing that existed at $t = 11.82T_F$ in figures 6(d) and 9(c, d). The $\rho = \rho_0$ isosurface at $t = 16.75T_F$ is similar to that shown in 6(d). The kinetic and potential energy spectra at $t = 16.75T_F$ are shown in figure 10. Here the degree of isotropization at small scales is very good. For wavelengths below 1 m, the difference between $E(k)/3$ and any of the component spectra is below 10%. Questions of the anisotropy in the buoyancy range and the degree of isotropy in the inertial range have been the subject of many studies, too many to try list here, but we refer the reader to van Haren, Staquet & Cambon (1996) and Gargett, Osborn & Nasmyth (1984) where further references may be found.

We will also use the spectra shown in figure 10 to discuss Lumley's (1964) theoretical model of the transition from buoyancy to inertial range. By considering how the flux of energy would change from one wavenumber band to the next in the kinetic energy spectrum, due to loss of kinetic energy to the potential energy, Lumley (1964) found a composite spectrum that represents in a continuous way the transition from the buoyancy range to the inertial range as a function of k. Since then, there have been several attempts at a complete theory along these lines, most notably by Phillips (1967), Holloway (1981, 1983) and Weinstock (1985), with an alternative approach taken by Gibson (1986). Following the notation of Holloway (1981) but ignoring, for the present, questions of the anisotropy in the buoyancy range, we can write

$$E_v(k) = C_K \epsilon^{2/3} k^{-5/3} + C_u N^2 k^{-3}, \tag{3.5}$$

$$PE(k) = C_o \epsilon_{pe} \epsilon^{-1/3} k^{-5/3} + C_\theta N^2 k^{-3}. \tag{3.6}$$

For large k the spectra are just the inertial-range forms that we used previously. For small k the spectra are of the buoyancy-range type given in equation (1.1) save for the possibility of the constant coefficient α taking different values in the two spectra: C_u and C_θ for the kinetic and potential energies respectively. In figure 10(a) we fit the component spectrum E_v with $1/3$ of the $E(k)$ given by equation (3.5), and in figure 10(b) the potential energy spectrum with (3.6). As before when matching with the asymptotic spectra, the match was made by eye. The selected curves are drawn in as the dotted lines in figure 10(a, b). The matches appear to be fairly good for scales well above the forcing and somewhat below the spectral cutoff.

Besides the kinetic and potential energy spectra, we can also find predictions for the buoyancy flux spectrum in both the theory of Lumley–Shur (cf. Lumley 1964, 1967; Phillips 1967; Weinstock 1985) and the theory of Holloway (1983, 1986). The modal spectrum of the buoyancy flux can be written as

$$-g\mathscr{R}\langle w_{\boldsymbol{k}}^* \rho_{\boldsymbol{k}}' \rangle / \rho_0. \tag{3.7}$$

If this quantity is positive, then for wavevector $\boldsymbol{k}$ there is conversion of potential energy to kinetic energy, and vice versa if it is negative. In figure 11(a), we plot the buoyancy flux spectrum from our simulation as a function of k. This is a time-averaged spectrum, where we have averaged over a period of $6T_F$, with time increment of $0.1T_F$. The time averaging is necessary to remove temporal fluctuations in the large scales. Note that the buoyancy flux spectrum is negative for large scales ($1 < k < 3$), and positive for smaller scales. This implies a transformation of kinetic to potential energy at large scales (closest to the forcing scale $k = \sqrt{2}$) and a transfer of potential to kinetic energy at all smaller scales.

The prediction of the Lumley–Shur theory for the buoyancy flux spectrum in the buoyancy and inertial ranges is

$$BF(k) = -2D\frac{\epsilon_0}{k_b}(1 + D(k_b/k)^{4/3})^{1/2}(k_b/k)^{7/3} \tag{3.8}$$

where k_b is as defined in (1.4) and D is a constant. Lumley (1964) assumed the buoyancy flux and hence D to be positive. In displaying his final result, Lumley incorporated D into his definition for k_b, but we will leave it explicit. Lumley's prediction of positive buoyancy flux through the buoyancy and inertial ranges is just the opposite of what we have found numerically for our wave-forced problem. All of the ingredients for an alternative prediction of the buoyancy flux are given in Holloway (1983); however, the buoyancy flux was not calculated in that paper. In Holloway (1986), we find a prediction for the buoyancy flux that, interestingly, can be either positive or negative depending on certain empirical constants. We have not been able to reproduce the buoyancy flux formula given in Holloway (1986), but in our Appendix, we provide a derivation of the buoyancy flux based on the theory of Holloway (1983, 1986). The resulting expression is identical in form to the Lumley–Shur result (3.8). However, in the derivation based on Holloway (1986), it is clear that D may be positive, negative or zero.

Since our observed buoyancy flux spectrum is positive through both the buoyancy and inertial ranges, it can be compared to the theoretical prediction given by (3.8) only by choosing a negative value for D. To define the constant D, we note that the wavenumber, where the buoyancy flux vanishes is determined by D. Here we shall choose D so that the zero value occurs at $k = 3.5$ (corresponding in our simulation to a wavelength of 5.7 m) since our buoyancy flux was found to vanish between $k = 3$
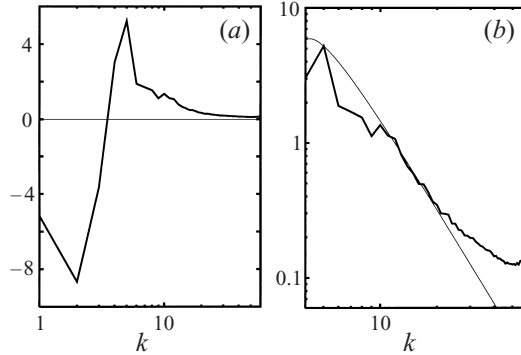
FIGURE 11. (*a*) The buoyancy flux spectrum averaged over 6 periods of the forcing, with 10 samples per period. (*b*) As in (*a*) but only the positive portion of the spectrum plotted in log-log format to compare with the theoretical spectrum of equation (3.8) with negative coefficient *D*. The result from the simulation is represented by the thick line, while the theoretical spectrum, based on $\epsilon_0 = \bar{\epsilon}$ where the overbar represents time averaging, is drawn as a thin line. All graphs in (*a*) and (*b*) are normalized by $\bar{\epsilon}/\kappa_b$.

and $k = 4$. The theory will apply only above this wavenumber, and we can think of this as the lower limit on the buoyancy range, or the upper wavenumber of the GM spectrum in the schematic shown in our introduction. To compute k_b, given by (1.4), we use the time-averaged dissipation rate $\bar{\epsilon}$. Thus all parameters in the theory are determined by the wavenumber where the buoyancy flux vanishes and the values of N and $\bar{\epsilon}$ (in this case $k_b \equiv (N^3/\bar{\epsilon})^{1/2} \approx 34.1$). The resulting theoretical buoyancy flux spectrum is compared in figure 11(*b*) to the results from our simulation. For wavenumbers in the buoyancy range, the match between theory and simulations is remarkably good. For the theoretical curve, the decay with k is approximately $k^{-7/3}$ for all k above about 10. The simulation data follows the theoretical curve fairly well up to about wavenumber 20, where the simulation spectrum begins to deviate from $k^{-7/3}$, and is clearly much shallower than this for $k \geqslant 30$. This shallowness of the simulation spectrum for k greater than about 30 is probably an indication that the buoyancy flux is not captured properly by the SGS model near the high-wavenumber cutoff. Recall that the cusp model viscosity grows rapidly with k for wavenumbers above about $k = 30$ and is largest at k_{max} (compare figure 2). This is just the range where our buoyancy flux spectrum becomes very shallow. It is very possible that the artificial damping of the high-k modes that the model performs to mimic transfer of energy beyond k_{max} does not allow for the proper treatment of the buoyancy flux in that region. But this is not unexpected for such a subgrid-scale model. It is remarkable that the theory does quantitatively so well in the buoyancy range considering that except for the point of zero value, there are no adjustable parameters in the theory.

Positive buoyancy flux for small scales has also been found in other simulations. In direct numerical simulations (i.e. simulations without subgrid-scale modelling) of forced stratified turbulence in both two and three dimensions, Holloway (1988), and Ramsden & Holloway (1992) showed that the buoyancy flux was negative only at large scales and positive at small scales. These results were interpreted as meaning negative buoyancy flux for $k < k_b$ (i.e. in the buoyancy range) and positive buoyancy flux for higher k. However, the forcing used in their simulations was spectrally fairly broad, and it would not be inconsistent with their results to say that the buoyancy flux was negative at the strongly forced modes and positive for smaller scales as

in our findings. Additionally, we have repeated our numerical simulations with a finite difference code using a Smagorinsky eddy viscosity, an independent test, and also found positive buoyancy flux through the buoyancy and inertial ranges. In their finite difference LES study of shear-driven stratified turbulence, Kaltenbach *et al.* (1994) also found positive buoyancy flux at small scale and negative at large scales, although we must note that the region of negative buoyancy flux in their simulations is spectrally very broad compared to ours. Perhaps this is just a result of differences in the type of forcing used. One can imagine that different forcing mechanisms capable of injecting a different mix of kinetic vs. potential energy at large scale would be able to extend the spectral range of negative buoyancy flux. Finally, we note that in two-dimensional flow simulations of the decay of a standing wave of just the type that we use for forcing our flow, Bouruet-Aubertot *et al.* (1996) found that the buoyancy flux was positive through most to the range that they identified with the buoyancy range, and also that the flux followed a $k^{-7/3}$ spectral law in a run with grid resolution 256^2 and a slightly steeper law at resolution 512^2 (note that those simulations did not include an inertial range).

4. Density-field structures

The main structure of interest in the buoyancy range evident in the density isosurfaces presented in the last section is the overturn produced by the curling over of the isosurface in a manner familiar from surface wave breaking. The overturning region shown in the breaking wave illustrated in figure 6(*c*) has a vertical scale of about 2 m. This is similar in size to overturns found in oceanographic measurements in the buoyancy range. Alford & Pinkel (2000) made an inventory of more than 2200 overturns. They found a median Thorpe scale, a measure of the vertical extent of the overturn, of 1.88 m. Since the observational data are primarily one-dimensional in space, it is difficult to form a three-dimensional image of those overturns. The ability to perform three-dimensional analysis of such structures is one of the benefits of numerical simulation.

Examining the full density field more thoroughly, we also find interesting structures of a rather different nature. These can be represented well by the deformations of the density surfaces that are the flat nodal surfaces of the forcing wave. We shall just refer to these surfaces as the nodal surfaces even when perturbed and deformed by eddies. The most basic motion of the fluid in the nodal surfaces is alternately toward and away from the centres of high strain as discussed in §2; however, the combination of the large-scale background straining motion and small-scale eddies produces localized deformations of the nodal surface that can result in overturning and mixing in a manner different from the overturns discussed in the last section. By plotting simultaneously three density isosurfaces (one 'nodal surface' and the most strongly perturbed isosurfaces above and below it) for a sequence of times during the forcing cycle, we can get some understanding of the nature, formation, evolution and fate of these structures, as shown in figure 12(*a–f*). We have shifted our view of the computational domain by an amount in the vertical sufficient to centre the upper 'nodal surface' in the image. Above and below the nodal surface, the most strongly displaced isosurfaces are shown. The upper and lower isosurfaces move vertically but always in opposite directions at any horizontal location. The combined effect of the motion of these surfaces above and below the nodal surface produces vertical 'dilation' and 'compression' centred on the nodal surface without producing large-scale sinusoidal displacement of that surface. In panels (*a*), (*b*) and (*c*), the upper/lower
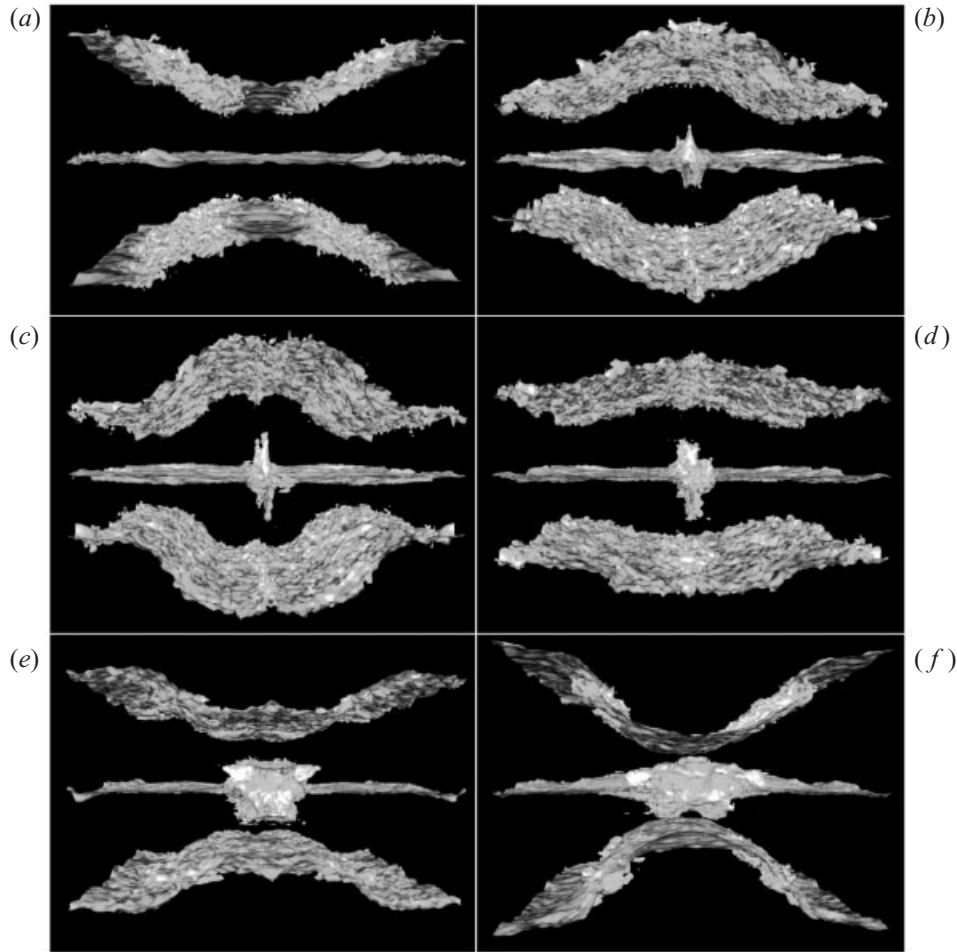
FIGURE 12. The evolution of three density isosurfaces ($g^*(\rho - \rho_0)/\rho_0 = 0, \pi/2, \pi$) showing the evolution of 'spouts' from a 'nodal surface' and their subsequent collapse with considerable broadening and mixing. Times represented are $t = 12.1 T_F$, $12.4 T_F$, $12.5 T_F$, $12.7 T_F$, $12.8 T_F$, and $13.1 T_F$.

surface is moving upward/downward in the middle of the domain (i.e. at $y = 0$, where y is the horizontal coordinate), and oppositely at the left and right ends of the domain. This is associated with the vertical straining of the nodal surface in the middle and at the left and right ends of the domain. In panel (b) the isosurface 'erupts' with elements moving up and down from a midline pointing into the plane. The eruption reaches its maximum extension when the upper and lower surfaces stop their motion, and reverses direction around the time of panel (c). At $y = 0$ on the nodal surface this is a time of maximum vertical dilational strain but zero strain rate (where $\partial w/\partial z$ is the vertical strain rate). The structures formed by these eruptions represent localized intrusions of heavy fluid into light fluid and vice versa. We shall refer to them as 'spouts'. As the upper and lower isosurfaces move back toward the nodal surface, the sense of straining motion is reversed and the spouts that were formed are flattened. This causes a spreading out of these structures, which in some cases results in tossing elements of the spouts to the right and left of the midline. This results in the kind of pattern seen in panel (e) which is in part an elongated horizontal structure as opposed
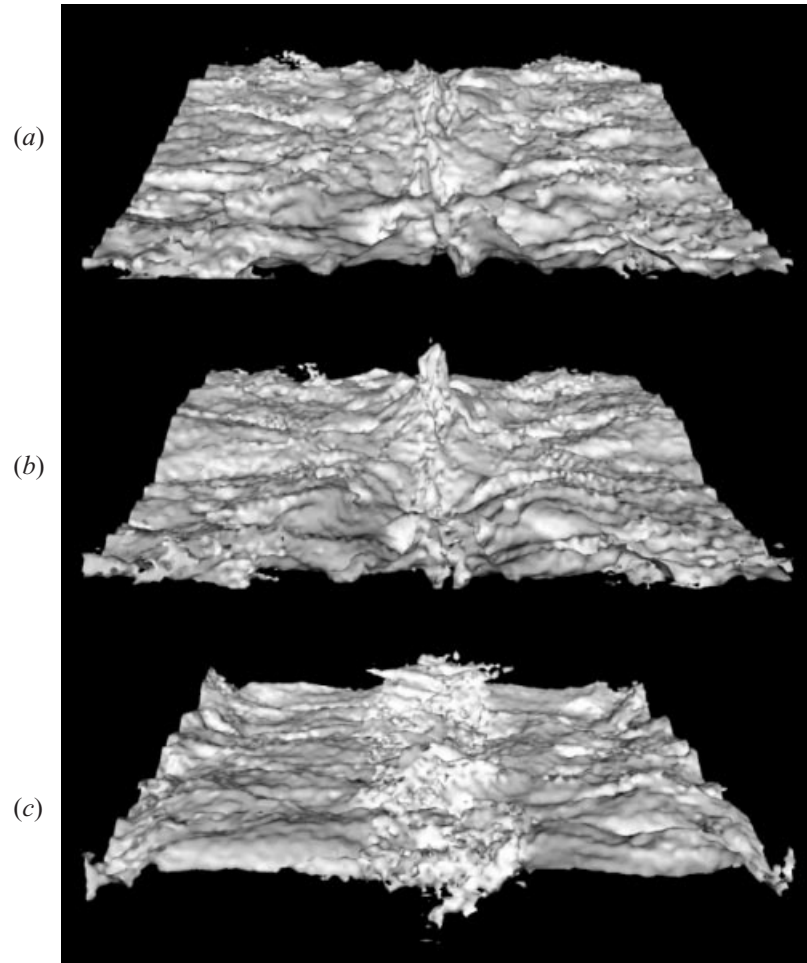
FIGURE 13. Visualization of the isosurface corresponding to one of the nodal planes of the forcing $(g^*(\rho - \rho_0)/\rho_0 = \pi/2)$ for a sequence of times during the formation of spouts. View taken along the x-axis. The time sequence is (a) $15.90 T_F$, (b) $16.04 T_F$ and (c) $16.32 T_F$.

to the elongated vertical structures originally produced during the vertically dilational phase of the large-scale straining motion. The final panel (f) shows the isosurface a short time after the upper and lower surfaces have again reversed their direction of vertical motion. This is a phase of the motion near to that of the initial panel (a), but now there is a mixed patch of fluid at the mid section ($y = 0$) of the nodal surface.

This production of spouts happens repeatedly, although not in each cycle of the forcing. Another example, from a later time, is given in figure 13 where we display the spouts on a larger scale to give a better idea of their physical structure. The isosurface starts relatively smooth (panel a), but then there is an eruption along a central line on the surface producing elongated vertical structures (panel b). In the final image (panel c), these structures have been elongated horizontally, producing regions of overturned fluid. Some of the spouts are elongated in the x-direction while some are nearly symmetric in x and y and appear like fingers of fluid.

Further details of one of these spouts and its environment are provided by contour plots of the full density field during one whole cycle of the forcing. Focusing on
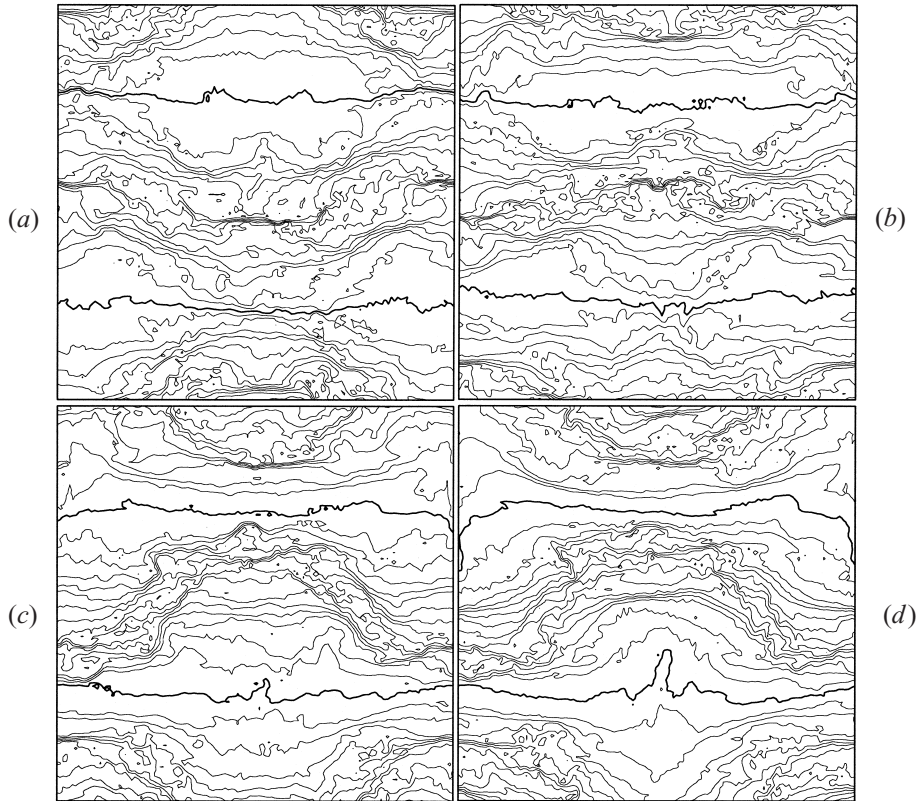
FIGURE 14. Contour plots of density in a vertical y, z cross-section through the domain during half of a forcing cycle to illustrate action of vertical dilational strain on the lower nodal surface. The origin is taken as the centre of each panel. The y- and z-axes are horizontal and vertical respectively. The thick contour lines correspond to isopycnals with the same densities as the nodal surfaces of the forced standing wave. In non-dimensional units these are $g^*(\rho - \rho_0)/\rho_0 = \pm \pi/2$. The sequence of times represented is (a) $15.61 T_F$, (b) $15.76 T_F$, (c) $15.90 T_F$ and (d) $16.04 T_F$.

the lower nodal surface near the middle of the domain ($y = 0$), we have broken the cycle up into the vertically dilational and compressional phases of the forcing (figures 14 and 15 respectively). Figure 14(a) corresponds to time $15.61 T_F$, which is just after the time of maximum vertical (compressional) strain, and is in the phase of vertical dilational straining motion (i.e. $\partial w/\partial x > 0$), with isosurfaces below and above the nodal surface retreating away from that surface. This continues in figures 14(b) and 14(c). In panel (c), we see the small perturbation that is being elongated vertically by the straining motion and this results in the spout seen in figure 14(d), which is roughly 2.5 m high and 0.75 m wide. Recall that our grid spacing is 15.6 cm, so that there are only about 5 grid points across the width of the structure making it resolved but close to the scale where the subgrid-scale model viscosity begins to grow with k (cf. figure 2). Thus the structure may be somewhat broader than it would appear in a higher resolution simulation. Note that at time of panel (d) ($t = 16.04 T_F$) the phase of the forcing is such that the neighbourhood of the spout is near maximum vertical (dilational) strain, which is evidenced by the large distortion of the contours surrounding the spout. Also, from the formula for the standing wave, we know that this instant corresponds to a time of approximately zero vertical strain rate. The next phase of the development is dominated by the vertically compressional
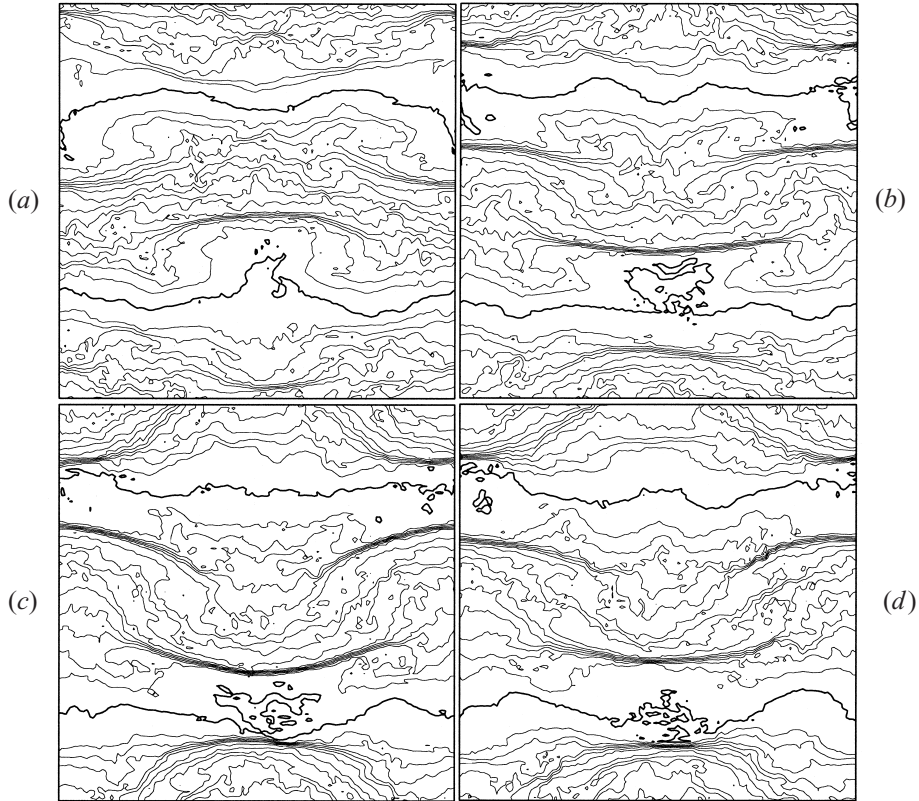
FIGURE 15. Contour plots of density in a vertical y, z cross-section through the domain during half of a forcing cycle to illustrate action of vertical compressional strain on the lower nodal surface. As in figure 14 except for the sequence of times: (*a*) $16.18T_F$, (*b*) $16.32T_F$, (*c*) $16.46T_F$ and (*d*) $16.60T_F$.

and horizontally dilational straining motion, and we follow the evolution in figure 15. Figure 15(*a*) shows the spout beginning to collapse under the influence of the vertically compressional motion, and the effect of the horizontally dilational motion is seen in panels (*b*) and (*c*) where the horizontal elongation of the spout is evident. Note that this horizontal elongation has deformed it into a structure that has regions of overturning and is, hence, convectively unstable. In the last panel, we have returned to approximately the same phase of the forcing as in 14(*a*), but the collapse of the spout has produced a region of mixed fluid with relatively low vertical density gradient, although very strong gradients appear just above and below the region where the spout had been.

To further illustrate the dynamics that create the spouts, we superimpose contour plots of vorticity ω_x and vertical strain $\partial w / \partial z$ on the density field illustrated in figures 14 and 15. The vorticity and strain fields are filtered at the 2 m level. The vorticity and strain rate reach their highest values at the smallest scales, where they are fairly isotropic. The creation of structures in the buoyancy range, however, is the result of the larger scale vortices that can have a coherent effect on the density field. We will specifically focus on the creation of the spout at time $16.04T_F$ (figure 14*d*). If we look at the vorticity and strain field, there is not much obvious correlation between the density structure and these fields because the vortices that create the spout have waned in strength by this time. It proves more illuminating to consider the vorticity
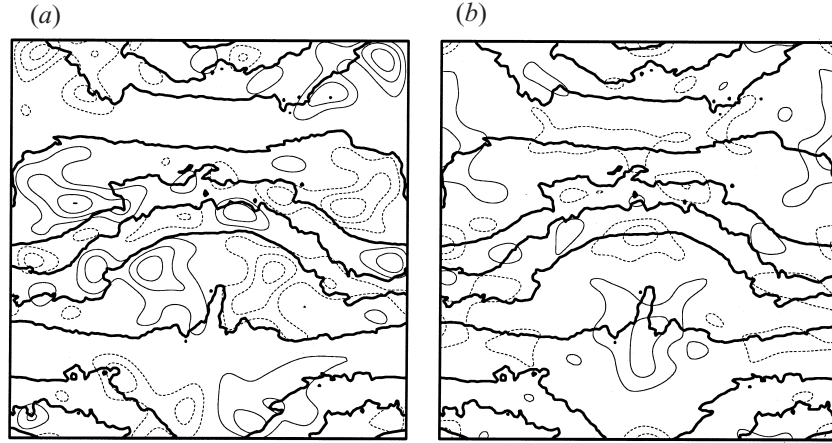
(*a*)   (*b*)

Figure 16. Contour plots of the density ρ/ρ_0 (thick lines) in a y, z cross-section at time $t = 16.04 T_F$, as in figure 14*d*, with superimposed vorticity and strain fields from $t = 15.9 T_F$ (see text). (*a*) Contour plot of ω_x, filtered at the 2 m scale, superimposed on the contours of density. The thin solid/dashed lines represent positive/negative contour levels (contour interval $1.1 S_G (20\,\text{m})$). (*b*) Contour plot of $\partial w/\partial z$, filtered at the 2 m scale, superimposed on the contours of density (contour interval $0.65 S_G (20\,\text{m})$).

and strain at a somewhat earlier phase in the evolution, say at time $15.90 T_F$ (the same time as in figure 14*c*). At that time the vortices that create the spout are near their maximum strength and it is their action that causes the growth of the incipient spout shown at $15.90 T_F$ into the fully developed structure that we see at time $16.04 T_F$. Thus in terms of the phase of the large-scale forcing, the development of the spout lags that of the vorticity field. In figure 16(*a*), we see that just above and to the right and left of the spout are a positive and a negative vortex. Since the vorticity is the source of the velocity field, we can say that this vortex pair creates a velocity field that advects the localized perturbation of the density surface away from its equilibrium position, creating the spout. We can also comment on the effect of the dipolar pair of vortices near the bottom of the figure. These create a velocity field that advects the density contours downward. The combined effect of the quadrupolar arrangement of vortices (the two adjacent to the spout and the two further down) is the creation of a region of low stratification just below the spout. The vertical strain-rate field associated with this vorticity distribution is shown in figure 16(*b*). There we see that the quadrupolar vorticity distribution near the spout creates a region of high positive strain rate, as anticipated in our earlier discussion. Similarly the phase of the horizontal strain $\partial v/\partial y$ (not shown) is such as to 'squeeze' the spout horizontally during its growth.

To summarize, we can say that the spouts originate from small-scale deviations of the nodal surface created by turbulent flow at the nodal surface. Once perturbations pull structures from the nodal planes vertically, these elements are subject to advection due to the large-scale straining motion of the forcing wave. At times and positions where the straining is highly dilational in the vertical, these deviations from the flat plane elongate vertically and narrow horizontally, forming spouts. Then, during the vertically compressional and horizontally dilational phase of the forcing, the spout is elongated horizontally creating regions of convectively unstable overturned fluid. Note that if the large-scale forcing were the only field acting on the spout, then the growth of the spout would simply have been reversed when the sense of the straining motion was reversed. Thus the presence of the eddy field must play an important

role in this irreversible process. The distortions of the spout by the eddy field are enhanced during the horizontally dilational phase of the evolution.

Finally, note that structures other than spouts at $t = 16.04$ can also be interpreted as created by the vorticity field after some lag. For example, there are some overturns in figure 16 that are associated with vortices of the correct sense of rotation to result in the localized curling over or plunging of the density surface. Thus the vorticity field filtered at the 2 m scale appears as a reasonably good predictor of the evolution of the density field structures that we have been discussing.

5. Sensitivity to the details of the SGS model

Before concluding we should discuss the sensitivity of our results to the precise form of the subgrid-scale model that we have used. First of all, let us note that we have compared the results obtained in our spectral simulations at resolution 128^3 with the same experiment performed with the same code at 64^3 and also with a finite difference code at 128^3 using a Smagorinsky type eddy viscosity and diffusivity. The results were essentially the same except that, as one would expect, in both comparison studies the observed structures were somewhat more diffuse than in the 128^3 spectral run.

Next, let us address the fact that we have incorporated in the model non-zero molecular viscosity and diffusivity. Recall that for the results shown above, we have used $v_{mol} = 0.01\ \mathrm{cm^2\,s^{-1}}$ and a molecular Prandtl number of 7, as would be reasonable values for the oceanographic problem. For the simulation used as an example here, this resulted in a Reynolds number of $O(10^5)$ based on the scale and maximum shear of the forcing wave. We have also run parallel studies in which we have set the molecular viscosity and diffusivity equal to zero (i.e. infinite Reynolds number runs). For the time $t = 11.68 T_F$ for which the energy spectra are shown in figure 9, the molecular viscosity is about 20% of the large-scale eddy viscosity $v_t(k = 1)$ and less than 8% of the cusp value $v_t(k = k_c)$. To test the sensitivity of the results given above to the presence of the molecular viscosity and diffusivity, we restarted the simulation at time $t = 11.26 T_F$ as an infinite Reynolds number run, that is with no molecular viscosity or diffusivity, and compared the subsequent evolution for six forcing periods to that of the finite viscosity case. Even at the end of the six forcing periods, there was very little difference between the two results in terms of the spectra or the density field structures. As we mentioned above, this is much in accord with the findings of Dornbrack (1998).

Before displaying some of the results for this comparison, let us also discuss another sensitivity test that we performed on the constants employed in the cusp model. The closure theory model for an infinitely long inertial range gives an eddy viscosity of the form (2.5) with coefficients $a_1 = 0.267$ and $a_2 = 9.21$, whereas we chose the coefficients $a_1 = 0.15$ and $a_2 = 5$ from the empirical model of Lesieur & Rogallo (1989). As a sensitivity test, we also ran a simulation in which we again started from $t = 11.26 T_F$ of the finite Reynolds number run and then continued it with the infinite Reynolds number model with coefficients $a_1 = 0.267$ and $a_2 = 9.21$. Although, there were no significant differences with the finite Reynolds number results after one forcing period, by the end of six forcing periods differences did become evident both in the energy spectra and the density isosurfaces.

To compare the evolution of the finite Reynolds number case with the eddy viscosity with $a_1 = 0.15$ and $a_2 = 5$ to the infinite Reynolds number case with the two types of eddy viscosities, we first consider the evolution of the enstrophy for all three runs.
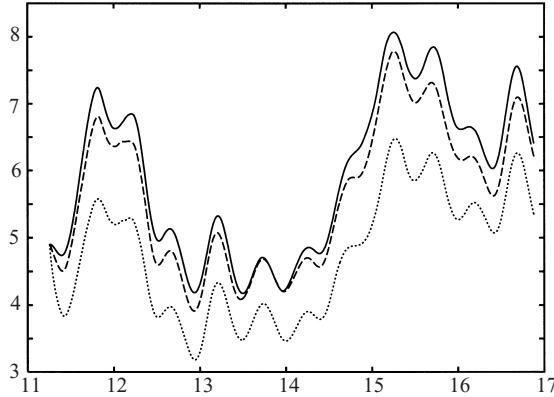
FIGURE 17. Graph of the evolution of the total enstrophy for three different parameterizations of the dissipation: the solid curve corresponds to the case with $a_1 = 0.15$, $a_2 = 5$, and $v_{mol} = 0$; the long-dashed curve corresponds to the case with $a_1 = 0.15$, $a_2 = 5$ and $v_{mol} = 0.01 \, \mathrm{cm^2 \, s^{-1}}$; and the short-dashed corresponds to the case with $a_1 = 0.267$, $a_2 = 9.21$ and $v_{mol} = 0$. The enstrophy is given in units of N^{-2}, and the unit for the horizontal time axis is the period of the cyclic forcing, that is $\sqrt{2} \, (2\pi/N)$.

This is shown in figure 17. The long-dashed curve corresponds to the finite Reynolds number case. First compare this with the enstrophy evolution for the $Re = \infty$ case with the $a_1 = 0.15$ and $a_2 = 5$ model drawn as a solid curve. The curves rapidly separate. The size of the difference fluctuates with the distance between the curves, sometimes vanishing, and the error does not exceed 8% over the $6T_F$ period of the test. On the other hand, the difference between the enstrophies for the two infinite Reynolds number models with different cusp parameters remains relatively large and varies by up to about 24% using the solid curve as the reference.

In figure 18, we show the $\rho = \rho_0$ density isosurface at time $15.3T_F$ for these tests. Frames (a) and (b) are respectively the infinite and finite Re cases, both using the $a_1 = 0.15$ and $a_2 = 5$ eddy viscosity model. There are some small differences that are noticeable, but basically both the large and small scales compare favourably. Figure 18(c) is from the infinite Re case with the $a_1 = 0.267$ and $a_2 = 9.21$ model. In comparison with (a) and (b) we notice some deviation on the large scale, but mainly we note that the surface texture is much smoother than in the other two cases.

The differences noted in the density isosurfaces are also born out by the energy spectra. Figure 19 shows the $E_v(k)$ and $PE(k)$ for each of the three runs at the $t = 15.3T_F$. There is essentially no difference in the spectra for two cases with the $a_1 = 0.15$ and $a_2 = 5$ eddy viscosity model. These are shown as thick solid curves. The spectra for the alternative eddy viscosity model ($a_1 = 0.2.67, a_2 = 9.26$) are indicated by dotted lines. In each panel, the $k^{-5/3}$ inertial range and the k^{-3} buoyancy model spectra are depicted by thin solid lines. The inertial-range spectra are fit to the data by choosing the Kolmogorov and Corrsin constants appropriately. On the other hand, the model buoyancy-range spectra in both panels are just given by $0.2N^2k^{-3}$ with no attempt to fit the data. In panel (a), we see that the thick curve follows the inertial-range model spectrum from about 1 m down to smaller scales. In that range, the data match the Kolmogorov inertial-range spectrum with a Kolmogorov constant of 1.55. The dotted curve however, tends to fall off more rapidly than the solid curve for scales smaller than about 60 cm. In panel (b), we see that the thick curve approaches the inertial-range model for scales smaller than about 60 cm and the inertial-range model
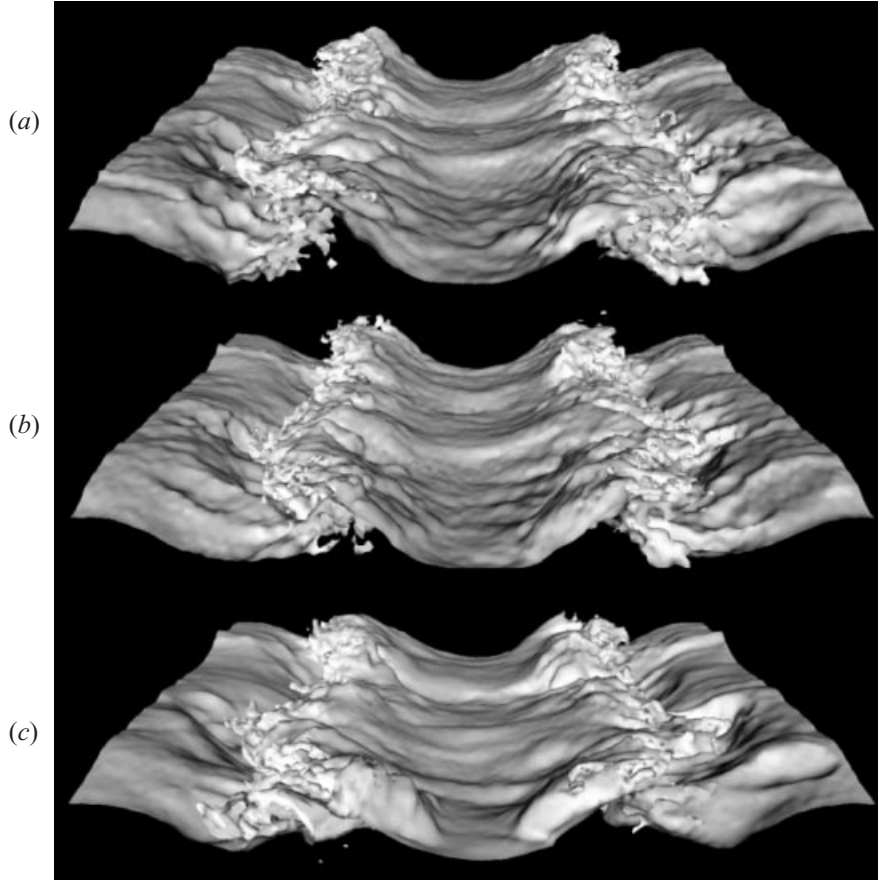
FIGURE 18. A breaking event visualized on the $\rho = \rho_0$ isopycnal at time $15.3 T_F$. The three surfaces shown are the same isopycnal level at the same time but for the three different dissipation parameterizations discussed in the text. (*a*) $a_1 = 0.15$, $a_2 = 5$, $\nu_{mol} = 0$, $\kappa_{mol} = 0$. (*b*) $a_1 = 0.15$, $a_2 = 5$, $\nu_{mol} = 0.01 \, \text{cm}^2 \, \text{s}^{-1}$, $Pr_{mol} = 7$. (*c*) $a_1 = 0.267$, $a_2 = 9.21$, $\nu_{mol} = 0$, $\kappa_{mol} = 0$.

that fits for these small scales has a Corrsin constant of 0.77. The dotted curve, on the other hand, falls off more steeply than the model inertial-range spectrum. Thus the spectra for the $a_1 = 0.267$ and $a_2 = 9.21$ model, follow the others fairly well for large scales; however, compared to the inertial-range models, they represent a deficit of energy for scales smaller than about 60 cm. This deficit results in the smoother texture noted in the corresponding density isosurface.

Finally, we shall discuss the sensitivity of our results to the choice of turbulent Prandtl number. In §2, we explained that we chose the specific value of 0.55 based on simulations of decaying turbulence. The variation of the potential energy spectrum as a function of Pr_t is a measure of the reasonableness of this choice. We have performed a series of numerical simulations starting from $t = 11 T_F$ in the run with $Pr_t = 0.55$, $\nu_{mol} = 0.01 \, \text{cm}^2 \, \text{s}^{-1}$ and $Pr_{mol} = 7$ discussed extensively in §§3 and 4. The earlier discussion in this section indicates that we should not expect much sensitivity of our results to the precise choice of the molecular values, and so we held those fixed while varying only Pr_t in our sensitivity study. In figure 20, we show the resulting potential energy spectra after evolution to $t = 16.8 T_F$ for five of the values of Pr_t that we find representative of this series of simulations. The time $t = 16.8 T_F$ is chosen because
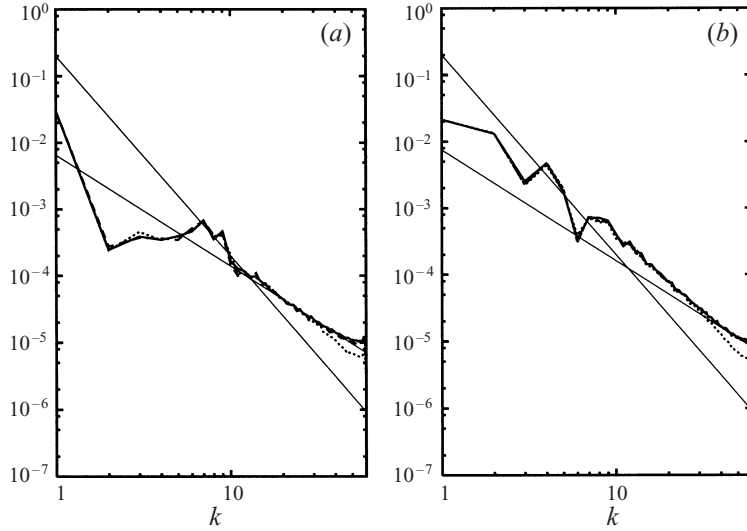
FIGURE 19. Energy spectra at time $15.3T_F$ from three different runs with different parameterizations of dissipation. The thick solid curves in each panel correspond to the two cases with $a = 0.15$, $b = 5$, and with $v_{mol} = 0$ and $v_{mol} = 0.01\,\mathrm{cm^2\,s^{-1}}$; and the dotted curves correspond to the case with $a_1 = 0.267$, $a_2 = 9.21$ and $v_{mol} = 0$. In each panel there is one thin line that corresponds to the appropriate $k^{-5/3}$ inertial-range model, and one corresponding to the buoyancy-range model $0.2N^2k^{-3}$. (a) Kinetic energy spectra for the v component of velocity. (b) Potential energy spectra.
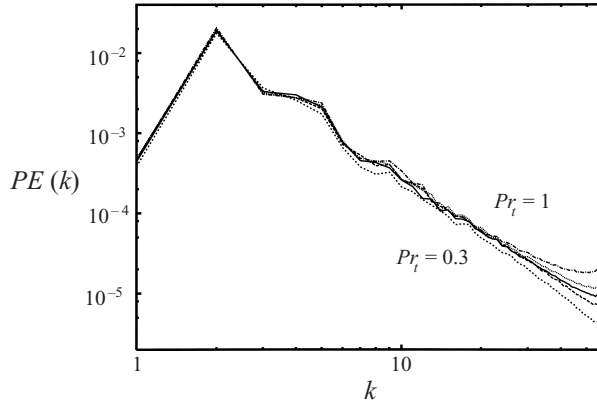

FIGURE 20. The potential energy spectrum at time $16.8T_F$ for each of five runs representing different choices of Pr_t. For all cases $v_{mol} = 0.01\,\mathrm{cm^2\,s^{-1}}$ and $Pr_{mol} = 7$. The values of Pr_t are 0.3 (short-dash), 0.4 (long-dash), 0.55 (solid), 0.6 (dots), and 1.0 (dot-dash). The correspondence of these values with the graphs is such that the lower the value of Pr_t, the lower the value of the energy at the upper wavenumber cutoff.

it is the same as in figure 10(b) where we demonstrated an excellent correspondence between the numerical potential energy spectrum obtained with $Pr_t = 0.55$ and the theoretical prediction. Here we again display $PE(k)$ for $Pr_t = 0.55$ as well as curves for two higher values $Pr_t = 0.6$ and 1.0 and two lower values $Pr_t = 0.3$ and 0.4. Looking at the high k end of the spectrum, we note that PE is larger for larger values of Pr_t. Note that the curve for $Pr_t = 0.3$ has an increase in the steepness of

the spectrum from about $k = 20$ toward higher wavenumbers, and this cannot be fit by the theoretical model (3.6), which shows the slope becoming steadily shallower as k increases. The curve for $Pr_t = 0.4$ has much more nearly constant slope for high k, but there is still a tendency, although slight, toward a steeper slope as k increases for k greater than about 20. We saw in figure 10(b) that the $Pr_t = 0.55$ curve matches the theoretical prediction fairly well except in the range near the cutoff, somewhat above $k = 50$ where there is some curl-up. This curl-up becomes systematically worse as Pr_t is increased as evidenced by the curves for $Pr_t = 0.6$ and 1. As we mentioned above, this curl-up indicates a degree of failure of the SGS model to properly mimic the transfer of energy to subgrid scales, near the high-wavenumber cutoff. Ideally, the model should be tuned to minimize this curl-up. These results indicate that a choice of Pr_t somewhere from 0.4 and 0.55 would be appropriate for our forced simulations, but also that variation in this range would not make significant differences except perhaps at the highest wavenumbers.

6. Discussion

We have seen that with the large-scale standing internal-wave type of forcing that we have used here, the expected spectral transition from a steep spectrum at large scales to a shallow inertial-range spectrum at small scales can be achieved, but only transiently during breaking events. How can we interpret this in terms of the buoyancy range of the ocean? If the spectral break does relate to breaking events, perhaps we should think of the oceanic spectra as an average of many different breaking events over a volume much larger than what is available to us with the methods employed here. Or perhaps a stationary spectrum with this transition could be observed in a cube of the ocean of 20 m width because the forcing to which it is subjected is composed of many different internal waves all interacting within this cube producing many more breaking events than we have with our single standing wave.

As for the structures that we have observed, the typical breaking patterns shown in figure 6(c, d) were very much what was to be expected given our familiarity with breaking surface waves, previous two-dimensional simulations, and the recent simulations of Andreassen *et al.* (1994), Dornbrack (1998) and Afanasyev & Peltier (1998). On the other hand, the spouts observed to form in regions of high vertical strain were unexpected. Their subsequent evolution that produced overturns of a type different from the classic breaking pattern could be of interest in analysing oceanic observations of overturns in regions of high strain (cf. Alford & Pinkel 2000). Although, a long-term standing wave is not the typical image one has for motions in the thermocline, it is certainly possible that waves passing through each other can create regions of high strain rate, and then it is possible that the isodensity surfaces could erupt with the kinds of spouts found here.

Appendix

Here we derive the result (3.8) for the theoretical buoyancy flux by starting from the basic relations of the Holloway (1983, 1986) theory. The equation for the evolution of the kinetic energy spectrum can be written as

$$\frac{\partial E}{\partial t} = T + BF - 2vk^2E \tag{A 1}$$

where E, T and BF are functions of k and t (cf. Frisch 1995). Here T is the nonlinear transfer of kinetic energy and $BF(k,t)$ is the spectrum of buoyancy flux. The term $\partial_t E$ can be assumed to vanish in a statistically stationary flow and also in our flow with oscillating forcing after sufficient time averaging. In the buoyancy and inertial ranges, the viscous dissipation can be neglected. Hence, in the statistically stationary buoyancy and inertial ranges we have $BF(k) = -T(k)$.

The transfer is the divergence of the flux of energy in spectral space (cf. Frisch 1995):

$$T = -\partial\epsilon/\partial k. \tag{A 2}$$

Here the energy flux ϵ is treated as a function of k and we will assume that ϵ becomes a constant ϵ_0 for sufficiently high wavenumbers in the inertial range. A model is needed for ϵ. The following four equations constitute such a model (Holloway 1986, equations 9, 10, 11 and 15 respectively):

$$\epsilon(k) = -a\mu^2\theta k^{r+1}\partial_k^r E, \tag{A 3}$$

$$\theta(k) = \frac{\mu}{\mu^2 + N^2}, \tag{A 4}$$

$$\mu(k) = b\epsilon^{1/3}k^{2/3}, \tag{A 5}$$

$$E = A\epsilon_0^{2/3}k^{-5/3}(1 + B(k_b/k)^{4/3}). \tag{A 6}$$

The order of the derivative r in equation (A 3) was left as an arbitrary positive (possibly fractional) number. For simplicity we will choose $r = 1$ in our derivation, but other choices give similar results as discussed below. The timescale θ is the corelation time for triad interactions, and it takes a form suggested by turbulence closure theory. Dimensional scaling based only on ϵ and k gives the relation (A 5) for the the nonlinear interaction rate or inverse eddy turnover time μ. We have introduced the constants of proportionality a and b which were left implicit in Holloway's equations. Positive ϵ may require negative values of a, depending on the value of r, while b can be assumed positive. In the energy equation, $A = C_K$ is the Kolmogorov constant and B is a positive empirical constant that takes into account that $k_b = (N^3/\epsilon_0)^{1/2}$ defines the transition wavenumber only approximately.

Taking (A 3) with $r = 1$ and substituting for θ from (A 4), we obtain

$$\epsilon = -\frac{a\mu^3}{\mu^2 + N^2}k^2\partial_k E. \tag{A 7}$$

Then substituting from (A 5) for μ, we have

$$b^2\epsilon^{2/3}k^{4/3} + N^2 = -ab^3k^4\partial_k E. \tag{A 8}$$

Next we substitute for E from (A 6), and after some algebra obtain

$$\epsilon = \epsilon_0\left(\tfrac{5}{3}abA + (3abAB - b^{-2})(k_b/k)^{4/3}\right)^{3/2}. \tag{A 9}$$

To achieve the correct limiting form for high k, we must choose $5abA/3 = 1$, and we can use this relation to fix a. Thus we have

$$\epsilon = \epsilon_0(1 + D(k_b/k)^{4/3})^{3/2} \tag{A 10}$$

where $D = (9B/5 - b^{-2})$. Therefore, depending on the size of B relative to b, this parameter D can be positive, negative or zero. Finally we can obtain $BF(k)$ in the buoyancy and inertial ranges from the relation $BF = -T = \partial_k \epsilon(k)$. This yields the desired result

$$BF(k) = -2D\frac{\epsilon_0}{k_b}(1 + D(k_b/k)^{4/3})^{1/2} \left(\frac{k_b}{k}\right)^{7/3}. \tag{A 11}$$

Other choices of the order of the derivative in (A 3) lead to the same result except for the coefficient of B in the expression for D. For example, if $r = 3$ then $D = (81/22)B - b^{-2}$. For fractional r, the coefficient of B would be more complicated, but can be expressed in terms of the Gamma function.

Thus we have demonstrated that the buoyancy flux predicted by the Holloway (1983) theory has the same analytical form as that of the Lumley–Shur theory. We must note, however, that the theories of Holloway and Lumley–Shur differ on important points. For example, in the Lumley–Shur theory, the relation between the kinetic energy spectrum and $\epsilon(k)$ is given by

$$E(k) = A[\epsilon(k)]^{2/3}k^{-5/3}, \tag{A 12}$$

whereas in the Holloway theory the relation is given by (A 3). Thus, in Lumley–Shur theory, the only way to obtain the correct form of the energy spectrum is to have $\epsilon(k)$ vary strongly with k in the buoyancy range. In contrast, in the Holloway theory the correct energy spectrum (A 6) can be obtained even if ϵ is constant in k. Furthermore, the energetics of the buoyancy and inertial ranges with negative buoyancy flux, as assumed in the Lumley–Shur theory, is very different from that with positive buoyancy flux, as allowed by Holloway's (1983, 1986) theory. With negative buoyancy flux, there is a transfer of kinetic to potential energy, and the kinetic energy flux $\epsilon(k)$ is a decreasing function of k. With positive buoyancy flux, the transfer is from potential to kinetic energy, in agreement with our numerical results for the wave forced turbulence, and $\epsilon(k)$ increases with k.

REFERENCES

AFANASYEV, Y. D. & PELTIER, W. R. 1998 The three-dimensionalization of stratified flow over two-dimensional topography. *J. Atmos. Sci.* **55**, 19–39.

ALFORD, M. & PINKEL, R. 2000 Observations of overturning in the thermocline: the context of ocean mixing. *J. Phys. Oceanogr.* **30**, 805–832.

ANDREASSEN, O., HVIDSTEN, P. O., FRITTS, D. C. & ARENDT, S. 1998 Vorticity dynamics in a breaking internal gravity wave. I. Initial instability evolution. *J. Fluid Mech.* **367**, 27–46.

ANDREASSEN, O., WASBERG, C. E., FRITTS, D. C. & ISLER, J. R. 1994 Gravity wave breaking in two and three dimensions. 1. Model description and comparison of two-dimensional evolutions. *J. Geophys. Res.* **99**, 8095–8108.

BENIELLI, D. & SOMMERIA, J. 1996 Excitation of internal waves and stratified turbulence by parametric instability. (4th International Symposium on Stratified Flows, Grenoble, France, 29 June–2 July 1994). *Dyn. Atmos. Oceans* **23**, 335–343.

BENIELLI, D. & SOMMERIA, J. 1998 Excitation and breaking of internal gravity waves by parametric instability. *J. Fluid Mech.* **374**, 117–144.

BLIX, T. A., THRANE, E. V. & ANDREASSEN, O. 1990 In situ measurements of the fine-scale structure and turbulence in the mesosphere and lower thermosphere by means of electrostatic positive ion probes. *J. Geophys. Res.* **95**, 5533–5548.

BOURUET-AUBERTOT, P., SOMMERIA, J. & STAQUET, C. 1995 Breaking of standing internal gravity waves through two-dimensional instabilities. *J. Fluid Mech.* **285**, 265–301.

BOURUET-AUBERTOT, P., SOMMERIA, J. & STAQUET, C. 1996 Stratified turbulence produced by internal wave breaking: two-dimensional numerical experiments. (4th International Symposium on Stratified Flows, Grenoble, France, 29 June–2 July 1994). *Dyn. Atmos. Oceans* **23**, 357–369.

BRISCOLINI, M. & SANTANGELO, P. 1992 Numerical simulations of three-dimensional homogeneous isotropic flows. In *Proc. Conf. on Parallel Computing: Problems, Methods and Applications* (ed. P. Messina & A. Murli) Elsevier.

CARNEVALE, G. F. & BRISCOLINI, M. 1999 Large eddy simulation of oceanic fine structure *'Aha Huliko'a, Internal Wave Modeling, Proc., Hawaiian Winter Workshop, University of Hawaii, January 19–22, 1999* (ed. P. Muller and D. Henderson). SOEST Special Publication.

CHOLLET, J.-P. 1985 Spectral closures to derive a subgrid scale modeling for large eddy simulations. *Lecture notes in Physics: Macroscopic Modelling of Turbulent Flows* (ed. U. Frisch, J. B. Keller, G. Papanicolaou & O. Pironneau), pp. 161–176. Springer.

DORNBRACK, A. 1998 Turbulent mixing by breaking gravity waves. *J. Fluid Mech.* **375**, 113–141.

FRISCH, U. 1995 *Turbulence.* Cambridge University Press.

FRITTS, D. C., ARENDT, S. & ANDREASSEN, O. 1998 Vorticity dynamics in a breaking internal gravity wave. 2. Vortex interactions and transition to turbulence. *J. Fluid Mech.* **367**, 47–65.

FRITTS, D. C., GARTEN, J. F. & ANDREASSEN, O. 1996 Wave breaking and transition to turbulence in stratified shear flows. *J. Atmos. Sci.* **53**, 1057–1085.

FRITTS, D. C., ISLER, J. R. & ANDREASSEN, O. 1994 Gravity wave breaking in two and three dimensions. 2. Three-dimensional evolution and instability structure. *J. Geophys. Res.* **99**, 8109–8123.

GARGETT, A. E. 1985 Evolution of scalar spectra with the decay of turbulence in a stratified fluid. *J. Fluid Mech.* **159**, 397–407.

GARGETT, A. E., HENDRICKS, P. J., SANFORD, T. B., OSBORN, T. R. & WILLIAMS, A. J. 1981 A composite spectrum of vertical shear in the upper ocean. *J. Phys. Oceanogr.* **11**, 1258–1271.

GARGETT, A. E., OSBORN, T. R. & NASMYTH, P. W. 1984 Local isotropy and the decay of turbulence in a stratified fluid. *J. Fluid Mech.* **144**, 231–280.

GARRETT, C. & MUNK, W. 1975 Space-time scales of internal waves: A progress report. *J. Geophys. Res.* **80**, 291–297.

GIBSON, C. H. 1986 Internal waves, fossil turbulence, and composite ocean microstructure spectra. *J. Fluid Mech.* **168**, 89–117.

GREGG, M. C. 1977 Variations in the intensity of small-scale mixing in the main thermocline (Pacific Ocean). *J. Phys. Oceanogr.* **7**, 436–454.

GREGG, M. C. 1989 Scaling turbulent dissipation in the thermocline. *J. Geophys. Res.* **94**, 9686–9698.

HAREN, L. VAN, STAQUET, C. & CAMBON, C. 1996 Decaying stratified turbulence: comparison between a two-point closure EDQNM model and direct numerical simulations. (4th International Symposium on Stratified Flows, Grenoble, France, 29 June–2 July 1994). *Dyn. Atmos. Oceans* **23**, 217–233.

HERRING, J. R. & METAIS, O. 1992 Spectral transfer and bispectra for turbulence with passive scalars. *J. Fluid Mech.* **235**, 103–121.

HOLLOWAY, G. 1980 Oceanic internal waves are not weak waves. *J. Phys. Oceanogr.* **10**, 906–914.

HOLLOWAY, G. 1981 Theoretical approaches to interactions among internal waves, turbulence and finestructure. In *Nonlinear Properties of Internal Waves, AIP Conf. Proc.* No. 76 (ed. B. J. West). AIP, New York.

HOLLOWAY, G. 1983 A conjecture relating oceanic internal waves and small-scale processes. *Atmos. Ocean* **21**, 107–122.

HOLLOWAY, G. 1986 Considerations on the theory of temperature spectra in stably stratified turbulence. *J. Phys. Oceanogr.* **16**, 2179–2183.

HOLLOWAY, G. 1988 The buoyancy flux from internal gravity wave breaking. *Dyn. Atmos. Oceans* **12**, 107–125.

ISLER, J. R., FRITTS, D. C., ANDREASSEN, O. & WASBERG, C. E. 1994 Gravity wave breaking in two and three dimensions. 3. Vortex breakdown and transition to isotropy. *J. Geophys. Res.* **99**, 8125–8137.

KALTENBACH, H.-J., GERZ, T. & SCHUMANN, U. 1994 Large-eddy simulation of homogeneous turbulence and diffusion in stably stratified shear flow. *J. Fluid Mech.* **280**, 1–40.

KRAICHNAN, R. H. 1976 Eddy viscosity in two and three dimensions. *J. Atmos. Sci.* **33**, 1521–1536.

LESIEUR, M. 1997 *Turbulence in Fluids*. Kluwer.

LESIEUR, M. & ROGALLO, R. 1989 Large-eddy simulation of passive scalar diffusion in isotropic turbulence. *Phys. Fluids* A **1**, 718–722.

LUMLEY, J. L. 1964 The spectrum of nearly inertial turbulence in a stable stratified fluid. *J. Atmos. Sci.* **21**, 99–102.

LUMLEY, J. L. 1967 Theoretical aspects of research on turbulence in stratified flows. *Atmospheric Turbulence and Radio Wave Propagation. Proc. Intl Colloquium, Moscow 1965* (ed. A. M. Yaglom & V. I. Tatarsky), pp. 121–128. Moscow: Nauka.

McEWAN, A. D. 1983*a* The kinematics of stratified mixing through internal wavebreaking. *J. Fluid Mech.* **128**, 47–57.

McEWAN, A. D. 1983*b* Internal mixing in stratified fluids. *J. Fluid Mech.* **128**, 59–80.

PATTERSON, G. S. & ORSZAG, S. A. 1971 Spectral calculations of isotropic turbulence, efficient removal of aliasing interactions. *Phys. Fluids* **14**, 2538–2541.

PHILLIPS, O. M. 1967 On the Bolgiano and Lumley–Shur theories of the buoyancy subrange. *Atmospheric Turbulence and Radio Wave Propagation. Proc. Intl Colloquium, Moscow 1965* (ed. A. M. Yaglom & V. I. Tatarsky), pp. 121–128. Moscow: Nauka.

RAMSDEN, D. & HOLLOWAY, G. 1992 Energy transfers across an internal wave-vortical mode spectrum. *J. Geophys. Res.* **97**, 3659–3668.

SIEGEL, D. A. & DOMARADZKI, J. A. 1994 Large-eddy simulation of decaying stably stratified turbulence. *J. Phys. Oceanogr.* **24**, 2353–2386.

TAYLOR, J. R. 1992 The energetics of breaking events in a resonantly forced internal wave field. *J. Fluid Mech.* **239**, 309–340.

WEINSTOCK, J. 1985 On the theory of temperature spectra in a stably stratified fluid. *J. Phys. Oceanogr.* **15**, 475–477.

WERNE, J. & FRITTS, D. C. 1999 Stratified shear turbulence: Evolution and statistics. *Geophys. Res. Lett.* **26**, 439–442.

WINTERS, K. B. & d'ASARO, E. A. 1997 Direct simulation of internal wave energy transfer. *J. Phys. Oceanogr.* **27**, 1937–1945.

WOODRUFF, S. L., SHEBALIN, J. V. & HUSSANI, M. Y. 1999 Direct numerical and large-eddy simulations of a non-equilibrium turbulent Kolmogorov flow. *ICASE Rep.* 99-45. NASA Langley Research Center (December 1999) Hampton, Virginia 23681-2199.